Popular summary for:

Tropical cumulus convection and upward propagating waves in middle atmospheric GCMs

T. Horinouchi, S. Pawson, K. Shibata, U. Langematz, E. Manzini, F. Sassi, R.J. Wilson, K.P. Hamilton, J. de Grandpre, and A.A. Scaife

Modeling the interactions between the middle atmosphere and the tropospheric climate system requires the development of complex models, including processes of relevance to both the hydrological cycle and to the chemistry of the ozone layer. While many of the basic components of these two systems are quite well understood and are captured with some degree of success in present day "middle atmospheric GCMs" (climate models which include the middle atmosphere), there are many processes that are not well characterized. For the troposphere, the need to parameterize sub-grid-scale cloud processes is well appreciated, and it is known that the models for convective systems that are used in GCMs are not fully consistent with the real atmosphere. In the tropical middle atmosphere, the large-scale dynamics are dominated by low-frequency oscillations: the quasi-biennial oscillation at low levels and the semi-annual oscillation near the stratopause and above. It is now realized that these low-frequency oscillations in the middle atmosphere are forced by high frequency, transient waves which propagate upwards from the troposphere. GCMs have long been unable to represent the low-frequency oscillations, although recent studies have shown that increasing the vertical resolution in some models, but not others, does allow them to generate quasi-periodic regimes with some characteristics of those observed. The present study shows that the gravity wave spectra generated by different models can vary considerably, in both the wavenumber and frequency domains, so that differences arise of more than one order of magnitude in the momentum transported by the waves from the troposphere to the stratosphere. It is further shown that these differences in eddy momentum transport are linked to the differences in the precipitation in the models, a result which arises because of the organization of convective systems on large space and time scales, even though each convective cell is very small. Models which use a primitive "moist convective adjustment" scheme for deep convection have a much larger space-time variability in precipitation, and hence in the tropical wave spectrum, than do models which use convection models that rely on large-scale balance assumptions. As well as characterizing the space-time variability in present-day climate models, this study gives a clear illustration of the link between parameterized convective systems in the troposphere and the large-scale, low-frequency dynamics of the middle atmosphere - as such, it provides an example of the complexities of the interdependence of different aspects of the climate system (in terms of both timescale and location in the atmosphere) and offers an additional criterion for the evaluation of the performance of convection schemes.

Tropical cumulus convection and upward propagating waves in middle atmospheric GCMs

T. Horinouchi,[1] S. Pawson,[2] K. Shibata,[3] U. Langematz,[4] E. Manzini,[5] M. A. Giorgetta,[5] F. Sassi,[6] R.J. Wilson,[7] K.P. Hamilton,[7,8] J. de Granpré,[9] and A. A. Scaife[10]

Short title: CUMULUS CONVECTION AND WAVES IN GCMS

For submission to JAS

copy - color figs are copied b/w on this copy.

Abstract. It is recognized that the resolved tropical wave spectrum can vary considerably between general circulation models (GCMs) and that these differences can have an important impact on the simulated climate. A comprehensive comparison of the waves is presented for the December-January-February period using high-frequency (three-hourly) data archives from eight GCMs and one simple model participating in the GCM Reality Intercomparison Project for SPARC (GRIPS). Quantitative measures of the structure and causes of the wavenumber-frequency structure of resolved waves and their impacts on the climate are given. Space-time spectral analysis reveals that the wave spectrum throughout the middle atmosphere is linked to variability of convective precipitation, which is determined by the parameterized convection. The variability of the precipitation spectrum differs by more than an order of magnitude between the models, with additional changes in the spectral distribution (especially the frequency). These differences can be explained primarily by the choice of different cumulus parameterizations: quasi-equilibrium mass-flux schemes tend to produce small variability, while the moist-convective adjustment scheme is most active. Comparison with observational estimates of precipitation variability suggests that the model values are scattered around the truth. This result indicates that a significant portion of the forcing of the equatorial quasi-biennial oscillation (QBO) is provided by waves with scales that are not resolved in present-day GCMs, since only the moist convective adjustment scheme (which has the largest transient variability) can force a QBO in models that have no parameterization of non-stationary gravity waves. Parameterized cumulus convection also impacts the nonmigrating tides in the equatorial region. In most of the models, momentum transport by diurnal nonmigrating tides in the mesosphere is larger than that by Kelvin waves, being more significant than has been thought. It is shown that the equatorial semi-annual oscillation in the models examined is driven mainly by gravity waves with periods shorter than three days, with at least some contribution from parameterized gravity waves; the contribution from the ultra-fast zonal wavenumber-1 Kelvin waves is negligible. These results provide a state-of-the-art assessment of the links between convective parameterizations and middle atmospheric

waves in present-day middle atmosphere-climate models, giving physical insight into the processes of wave generation and the indirect importance of the cumulus scheme to the climate of the middle atmosphere.

1. Introduction

Vertically propagating waves from the troposphere play important roles in the equatorial middle atmosphere. The horizontal momentum carried by high-frequency transient waves is deposited as the waves are damped in the middle atmosphere, providing a forcing for the low-frequency oscillations that dominate the circulation. The quasi-biennial oscillation (QBO) in the lower and middle equatorial stratosphere is driven by the interaction between the mean flow and upward propagating waves of various spatial scales [Lindzen and Holton, 1968; Holton and Linden, 1972; Dunkerton, 1997]. At higher levels, the semiannual oscillation (SAO) is partially driven by similar interactions [e.g., Holton, 1975; Holton and Wehrbein, 1980]. Furthermore, vertically propagating waves affect constituent transport in the equatorial middle atmosphere [Shepherd et al, 2000; Fujiwara et al, 1998].

As discussed below, many studies have isolated waves in the equatorial middle atmosphere of general circulation models (GCMs) and shown that these waves play a role in the simulated climatologies. However, the temporal and spatial structure of these waves can differ among models, with important implications for driving the middle atmospheric circulation. While this point is important when interpreting GCM simulations, the differences between present-day models has not been characterized in any detail. To investigate them requires a careful comparison of high-frequency output from models; the results of such a study are presented here.

The waves observed in the equatorial middle atmosphere have wide variety of horizontal scales. These range from planetary-scale Kelvin waves [Wallace and Kousky, 1968; Hirota, 1978; Salby et al., 1984] and synoptic-scale mixed Rossby-gravity waves [Yanai and Maruyama, 1966], down to mesoscale gravity waves [Pfister et al, 1993] with spatial scales of O(1000)-O(10) km. It is now widely supposed that most of these waves are excited in the troposphere, mainly though cumulus convection [e.g., Salby and Garcia, 1987; Pfister et al., 1993; Alexander et al., 1995]. Even though each convective tower has a horizontal scale of O(1)-O(10)km, cumulus convection shows organization over various horizontal distances, ranging from the mesoscale to the planetary scale,

enabling a broad spectrum of waves to be excited by cumulus convection.

As the dominant low-frequency variation in the equatorial lower and middle stratosphere, the QBO has impacts on the tropical upper stratosphere and mesosphere and on the higher latitudes [see the review by Baldwin et al., 2001]. It also impacts the transport of trace gases, both directly through its associated mean meridional circulation and indirectly through its impacts on extratropical Rossby waves. Analyses of ozone variability and trends typically include the signature of the QBO [e.g., Randel et al., 1996]. Representation of the QBO is thus an important requirement if model studies of climate and its interaction with ozone are to be performed for the purposes of studying climate change and variability. However, the QBO has been captured in only a few GCMs, and the roles of resolved and parameterized waves remain unclear. Some GCM simulations of the QBO are now discussed, with the goal of expressing some of the uncertainties in the forcing mechanisms: these are some of the main motivations for performing this research.

The first GCM simulation of the QBO was reported by Takahashi [1996] using the CCSR/NIES AGCM. By using the T21 horizontal resolution (triangular truncation with the maximum total wavenumber equal to 21), they obtained a QBO-like oscillation when the vertical grid spacing was set to as fine as 500 m and the horizontal diffusion coefficient was lowered by an order of magnitude from standard values. Horinouchi and Yoden [1998] obtained a QBO-like oscillation in an aqua-planet GCM with a finer horizontal resolution. In both of these simulations, the QBO-like oscillations were driven by resolved waves with horizontal wavelengths on the order of a few thousand kilometers. In subsequent GCM simulations of the QBO, however, the relative contributions from resolved and parameterized waves vary among models. Resolved waves are solely responsible in the simulated QBO by Hamilton et al [2001] and those by Takahashi and his colleagues [e.g., Takahashi et al., 1997; Takahashi, 1999], while the parameterized wave forcing contributed about 50% of the forcing in the model of Giorgetta et al. [2002] and about two thirds of the forcing in that of Scaife et al. [2000].

There are presently insufficient observations to determine the wavelengths that

dominate the forcing in the real atmosphere. Historically, in the absence of observations of gravity waves, it was supposed that the QBO is driven mainly by planetary-scale Kelvin waves and synoptic-scale Rossby-gravity waves [Holton and Lindzen, 1972]. However, it was revealed that the momentum transport due to these waves is not sufficient [Lindzen and Tsay 1975; Dunkerton, 1991] to drive an oscillation with the amplitude and periodicity observed. Thus, it was proposed that gravity waves with wavelengths of up to a few thousand kilometers contribute more than the two larger scale waves [Dunkerton, 1997]; this is the case in the simulation by Horinouchi and Yoden [1998]. However, it is still an open question whether further small-scale (i.e., mesoscale) gravity waves play an indispensable role in the forcing of the QBO [e.g., Alexander et al., 1995; Baldwin et al., 2001]. If they are important, a significant portion of the QBO forcing comes from sub-grid-scale gravity waves, compared to the typical resolutions of GCMs used of multi-annual simulations of the middle atmosphere-climate system. If that is the case, it should not be regarded as a failure if a GCM does not produce a QBO without a parameterization of subgrid-scale traveling gravity waves.

Wave excitation by cumulus convection occurs mainly through its diabatic effect, at least for waves whose horizontal wavelengths are larger or comparable to O(1000) km [Hayashi, 1976; Itoh, 1977; Salby and Garcia, 1987; Manzini and Hamilton, 1993; Horinouchi and Yoden, 1996]. In GCMs, the effect of subgrid-scale cumuli on grid-scale dynamics is parameterized as thermal forcing, which originates ultimately in latent heating and cooling due to condensation and evaporation. Therefore, in principle, if the time-dependent grid-mean thermal effect of cumulus convection is reproduced well in a GCM, the model can have quantitatively realistic vertically propagating waves in its equatorial middle atmosphere. However, there are a number of factors that affect wave propagation in GCMs, such as vertical resolution [Boville and Randel, 1992; Takahashi, 1996; Nissen et al., 2000] and eddy diffusivity [Takahashi, 1996]. Since the study of Takahashi [1996] these two factors had been considered to be dominant. Also, the mean flow, whose bias is not necessarily due to that in wave-mean flow interaction, obviously affects wave propagation.

The simulations mentioned above in which the QBO is driven solely by resolved waves used the moist convective adjustment (MCA) scheme [Manabe et al., 1965] to represent the effects of cumulus convection. Recently, Ricciardulli and Garcia [2000; hereinafter RG2000] examined the variability of diabatic heating due to parameterized cumulus convection in the National Center for Atmospheric Research (NCAR) Community Climate Model, Version 3 (CCM3) GCM. They showed that the variability produced by the standard convective parameterization of the model, the Zhang and McFarlane (ZM) [1995] scheme, is much smaller than that produced by the Hack [1994] scheme, which was the standard parameterization for the previous version of the model, CCM2. They further inferred momentum flux associated with convectively generated waves by using the idealized linear calculation method of Salby and Garcia [1987], and showed that estimated momentum flux is much smaller with the ZM scheme than with the Hack scheme. They also showed that the variability of convection in the latter case is close to that modeled by Horinouchi and Yoden [1998]. Therefore, whether the QBO is reproduced in a GCM could depend on which convective parameterization is used. (It should be stressed that neither CCM2 nor CCM3 capture a QBO-like oscillation.) By comparing with space-time spectra of diabatic heating inferred by Bergman and Salby [1994] from satellite cloud imagery, RG2000 suggested that the variability obtained with the Hack scheme is more realistic than the ZM scheme. This implies that the QBO may be driven mainly by waves on the scales that are resolved by the T42 resolution, but that require higher vertical resolution to adequately capture the wave-mean flow interactions that force the oscillations. However, Horinouchi [2002] recently showed that the method of RG2000 may substantially overestimate the convective variability.

The quest to understand the forcing of the SAO, especially the forcing of its westerly phase, has a similar history to that of the QBO. It was first proposed that Kelvin waves produce its westerly phase [Holton, 1975], but Hitchman and Leovy [1988] deduced that planetary-scale (wavenumber 1-3) Kelvin waves provide only 30 to 70% of the total westerly forcing near the stratopause, inferring that smaller-scale gravity waves provide the remaining forcing. Using a mechanistic-type of model, with convective

heating prescribed with guidance from observations, Sassi and Garcia [1997] found that large-scale waves provide about half of the westerly forcing, the remainder coming from intermediate-scale (zonal waves 4 to 15) waves. On the other hand, Hamilton and Mahlman [1988] showed that in the SAO simulated with the "SKYHI" GCM, eastward acceleration is due to gravity waves with a broad distribution of scales and that the role of planetary-scale Kelvin waves is fairly minor. Ray et al. [1998] analyzed the United Kingdom Meteorological Office (UKMO) global assimilation dataset to estimate the forcing of the SAO, showing that the westerly forcing by resolved waves (including Kelvin waves) is far from sufficient to drive the SAO. They also showed that a parameterization of non-stationary mesoscale gravity waves can quantitatively mimic the missing forcing. In summary, the relative contribution of various scales of waves to the westerly forcing of the SAO is still an open question, as it is for the QBO.

Unlike the QBO, most GCMs with adequate vertical extent do simulate an SAO signal. However, it is because the easterly phase of the SAO is driven by inter-hemispheric transport of angular momentum during the solsticial seasons [Holton and Wehrbein, 1980] rather than by waves. Close inspection reveals that the simulated SAOs differ greatly in magnitude [e.g., Amodei et al., 2001], often varying between weak and strong easterlies instead of easterlies and westerlies. That is, it is the westerlies and their strength that vary most greatly among models.

Tropospheric latent heating due to cumulus convection has a diurnal cycle, and it accordingly excites atmospheric tides [Lindzen 1978; Hamilton 1981]. Although radiative heating is the dominant source of migrating tides, latent heating contributes significantly to the excitation of non-migrating tides [Tokioka and Yagai, 1987; Lieberman and Leovy, 1995; Williams and Avery, 1996; Hagan et al., 1997]. Idealized and general circulation models have been used to study the impacts of the tides on the zonal momentum budget, and it has been shown that they are important in the lower thermosphere [e.g., Miyahara et al., 1993], and that they may play some roles in the upper mesosphere [Lieberman and Leovy, 1995; Portnyagin and Solovieva, 1997].

A number of GCMs are currently used to study the middle atmospheric processes

and climate. Each model consists of a number of components such as the dynamical core, radiation, convective parameterization, surface processes, and external conditions, each of which can be represented in many ways. Complete evaluation of our ability to simulate the atmosphere requires comprehensive intercomparison of various aspects of the GCMs. For this purpose, the project "Stratospheric Processes And Their Roles in Climate" (SPARC) initiated a subproject "GCM-Reality Intercomparison Project for SPARC" (GRIPS; Pawson et al., 2000). This study is conducted within GRIPS, and its purpose is to investigate resolved waves in the equatorial region of various GCMs. The following specific issues are investigated:

1. Quantification of various kinds of resolved waves in the equatorial middle atmosphere of currently used GCMs
2. How and to what extent do the waves differ among the GCMs?
3. How do the results compare with observations?
4. How can the difference be explained in terms of the choice of model components and their settings?
5. How does the difference affect simulated mean flow?

The results of this study will also be useful to the studies of the parameterization of subgrid-scale gravity waves (GWs). Some studies investigated GW parameterizations only by examining simulated mean states. However, a GW parameterization works in combination with resolved waves. Therefore, a GW parameterization could be judged mistakenly, if the resolved waves are not realistic. This study will also be useful to improve convective parameterizations, since a good deal of investigation is made in terms of their characteristics to excite vertically propagating waves.

The rest of the paper is organized as follows. The models used in this study are summarized in Section 2. Results are shown in Section 3. A discussion regarding cumulus parameterization is made in Section 4, and conclusions are drawn in Section 5. Appendix describes the spectral method used in the study.

2. Models

The GCMs used in this study Table 1 are participants in the GRIPS evaluation. Table 1
Several of these have been further developed since the initial comparison of their mean states was presented [Pawson et al., 2000]. Two of the GCMs, the MACCM3 and the FVCCM replace the model versions from NCAR and NASA's Data Assimilation Office used in the earlier GRIPS comparison; almost all of the models in this paper have been updated in some way since the study of Pawson et al. [2000]. Data collection for this study began in 1998, so the most recent versions of all models are not used; this does not impact the conclusions of the work, but does point to the need for careful documentation of the models used. In addition to the GRIPS models, data from an aqua-planet model (AGCM5-HY98) have been used [as in Horinouchi and Yoden, 1998].

Table 2 shows specification of the model grids. Many of them are spectral with Table 2
triangular truncation (T21 for the FUB model; T32 for the CMAM; T42 for the MRI/JMA98, MAECHAM4, and AGCM5-HY98 models). Although the standard dynamical core of the NCAR CCM3 is also spectral, neither of the two variations used here are spectral; the MACCM3 model uses semi-Lagrangian dynamical core based on the spectral grid [Williamson and Olson, 1994], and the FVCCM model uses a completely new dynamical core developed by Lin and Rood [1996], which is based on the finite-volume method and uses both the C- and D-grids. The other models use grid methods; the UKMO model has the so-called B-type grid configuration [e.g., Arakawa and Lamb, 1977; Haltiner and Williams, 1980] and the SKYHI has the A-type grid configuration. Both in terms of horizontal and vertical resolutions, the coarsest among the models is the FUB model, and the finest is the SKYHI-N45L80. The spectral T42 is a typical horizontal resolution among the models. Note that many of the GRIPS GCMs have finer resolution than they had when studied by Pawson et al. [2000].

Table 3 briefly summarizes physical parameterizations in the models and some Table 3
other information. Of particular interest among many kinds of parameterizations is the cumulus parameterization. The MRI/JMA98 model uses the Arakawa-Schubert scheme [Arakawa and Schubert, 1974] with a prognostic closure [Randall and Pan,

1993], convective downdraft and some simplification [see Shibata et al 1999 for details]. The FUB model uses the Kuo scheme [Kuo, 1974] with the modification by Tiedtke et al. [1988]. The MAECHAM4 model uses the Tiedtke scheme [Tiedtke, 1989] with the modification by Nordeng [1994], where an important modification is that the cloud-base mass flux is related to convective available potential energy rather than large-scale moisture supply used in the original scheme. The UKMO model uses the Gregory and Rowntree (GR) [1990] scheme. The MACCM3, FVCCM, and CMAM model use the Zhang-McFarlane [1995] scheme, referred to as "ZM." More details on the cumulus parameterizations in the models are presented in Section 5.

With regard to the parameterization of unresolved gravity waves (GWs) in the models considered, there are three cases: No parameterization, the parameterization of orographic (zero phase speed) gravity waves [McFarlane, 1987], and the parameterization of orographic and non-orographic (non-zero phase speed) gravity waves, which are separate schemes. Since orographic waves have stationary phase speeds they do not force equatorial mean-flow oscillations. For this reason, it is really only the parameterization of non-orographic gravity waves which plays a role in the driving of equatorial mean-flow oscillations by unresolved gravity waves. A few of the models have such parameterizations: the Hines [1997ab] scheme in the MAECHAM4 model, the Warner and McIntyre (WM) [1999] scheme in the UKMO model, and a Lindzen[1981]-type parameterization of arbitrary non-stationary gravity waves with a few discrete phase speeds in the MACCM3 [Sassi et al, 2002]. All the models except for the SKYHI and AGCM5-HY98 have the diurnal cycle in solar insolation, and all but the AGCM5-HY98 have climatological annual cycle in sea surface temperature. Sea-surface temperature (SST) is not unified among models. AGCM5-HY98, which has an experimental setup by Horinouchi and Yoden [1998], is an aqua-planet model with uniform SST.

For the GCMs, data between 30°S and 30°N were collected every three hours for a three-month period of December, January, and February (Table 3). As for the AGCM5 that was run without seasonal cycle, an arbitrary 60-day period was chosen. The physical quantities collected were zonal and meridional winds, vertical pressure

velocity (Dp/Dt), temperature, and total precipitation rate at the surface (including both the parameterized and resolved components). The rainfall rate is averaged over 3 hours. The three-dimensional output was interpolated onto constant pressure surfaces close to the vertical grid points of the model. For most of the models, data above 100 hPa were not interpolated, since they use the hybrid coordinate. The exceptions are MRI/JMA98 model, where the data were interpolated to the standard vertical levels for the original GRIPS data collection [Pawson et al., 2000], and AGCM5, which uses the sigma coordinate.

3. Results

3.1. Mean state

Most models have SAOs in the upper stratosphere and mesosphere. Time-height section of the zonal mean zonal wind near the equator is shown in Fig. 1 for three typical cases of the SAO (MRI/JMA98, MACCM3, and SKYHI-N30L40). For other models, only mean zonal winds of January are shown in the lower-right panel. The MRI/JMA98 model has a weak SAO (upper-left panel), where not only the westerlies but also the easterlies are weak, which suggests that the inter-hemispheric angular momentum transport in solsticial seasons is weak in the model. Among the two CCM3 variants, the FVCCM also has a weak SAO with only seasonally varying easterlies, while the MACCM3 has clear descending westerlies. The westerly phase of the SAO in the latter is mainly forced by the non-stationary GW parameterization, which is absent in the former. The MAECHAM4 and UKMO model, which also have non-stationary GW parameterizations, have descending westerlies too (not shown). The SKYHI-N30L45 model also produces distinct westerly phase of the SAO, although it does not have a non-stationary GW parameterization. The model reproduces the observed amplitude minimum of the SAO in the lower mesosphere. Generally speaking, however, one cannot expect to see the separation between the stratopause and mesopause SAOs in middle atmospheric GCMs with tops at around 0.01 hPa (below the mesopause). The separation is not seen in the other models. Interestingly, the SAO in SKYHI-N45L80

Fig. 1

is less realistic than that in SKYHI-N30L40 and does not have the separation [see Hamilton et al., 2001]. It should be noted that modeling the SAO is tied to the problems of modeling the QBO. The QBO, if present in a GCM, exerts filtering on the wave spectrum propagating upward across the QBO domain before reaching the shear levels of the SAO. This might explain the difference between the results of SKYHI-N30L40 and SKYHI-N45L80.

Three of the models (UKMO, SKYHI-N45L80 and AGCM5) have spontaneous QBO-like oscillations in the lower stratosphere as indicated in Table 3. The zonal mean wind in the lower stratosphere of the other models is weak easterly. The AGCM5 and SKYHI-N45L80 have an oscillation with a period of a little more than a year [Horinouchi and Yoden, 1998; Hamilton et al, 2001]. Hamilton et al [2001] showed that a noticeable oscillation appears in the lower stratosphere when a 80-layer vertical grid configuration and a sufficiently fine horizontal resolution were used, while no QBO-like oscillation was produced with the 40 layer vertical grid, which had been used for many years, regardless horizontal resolution. To examine the contrast between the cases with and without QBO in the SKYHI, both cases are examined in this study (SKYHI-N30L40; SKYHI-N45L80). The third model, the UKMO model, has a QBO with a realistic period of about 2 years.

Figure 2 shows horizontal distribution of precipitation between 30°N and 30°S averaged over a December, January, and February (DJF) period, for which waves and cumulus convection will be analyzed in what follows. Also shown is a 13-year climatology from the Global-Precipitation-Climatology-Project (GPCP) combined satellite-gauge precipitation estimate [Huffman et al., 1997]. Climatologically, the South-Pacific Convergence Zone (SPCZ) has active cumulus convection in this period of year, and the Pacific Inter-Tropical Convergence Zone (ITCZ) has weaker convective activity. However, the two SKYHI results do not show a clear SPCZ. It is a consequence of the use of the MCA scheme, which tends to produce precipitation around the equator [Numaguti, 1993]. Note that the AGCM5 is an aqua-planet model, so such a comparison is not possible. The MAECHAM4 model produces too strong SPCZ and too weak ITCZ.

Figure 2

In the FUB and CMAM models, the separation of ITCZ and SPCZ is not clear in the west of datelines, which might be due to their coarse horizontal resolutions. The models that were not mentioned above have relatively realistic distributions of precipitation. Figure 3 shows zonally averaged mean precipitation of the period. Biases mentioned above are clearly seen in the zonal mean precipitation. It is clear in this figure that the ITCZ in the models with the MCA scheme is too close to the equator.

Figure 3

3.2. Wavenumber-frequency spectra

In order to investigate the sensitivity of resolved waves to parameterized cumulus convection, two dimensional, zonal wavenumber-frequency spectra were calculated from modeled precipitation and dynamical quantities. See Appendix for the definition of spectra. Here, precipitation is used to represent vertically integrated diabatic heating due to cumulus convection in GCMs. For a first approximation, it is a good indicator of the thermal forcing of vertically propagating waves.

The left panels in Figure 4 shows the results for precipitation between 10°N and 10°S. Here, frequency, ω, is positive definite, and zonal wavenumber, s, is positive for eastward, and negative for westward, propagating disturbances. Plotting is made in the "energy-content" form, in which the spectra were multiplied with wavenumber and frequency, with these axes scaled logarithmically. Therefore, high frequency and/or wavenumber components are emphasized compared with conventional plots. Note that the energy-content display is desirable to assess relative importance of different wavenumber and/or frequency ranges. It is because it is practical to take wavenumber/frequency ranges with logarithmic interval such as $s = 1$ through 3 versus $s = 100$ through 300, not versus $s = 101$ to 103. The color levels are set logarithmically such that the difference between adjacent two levels corresponds to a difference of an order of magnitude. The two dimensional precipitation spectra are compressed into one-dimensional frequency spectra in Fig. 5 by integrating with respect to wavenumber (for both positive and negative values). The plot is made in the log-log coordinate without multiplying ω. Since the figure, therefore, is not drawn in the energy-content

Figure 4

Fig. 5

form, comparison of relative contributions of different frequency ranges, if desired, should be made along lines with the slope of -1 shown by dotted lines.

The overall power of the precipitation in the models with the MCA scheme (SKYHI, AGCM5) is significantly larger than those with any other cumulus parameterization (Figs. 4 and 5). Note that these models were run without the diurnal cycle of solar insolation. With respect to frequency, broad peaks were found between 0.2 and 0.5 cycles per day (cpd), while the power is largest around the highest wavenumbers resolved properly. The latter is because the precipitation due to the MCA scheme is dominated by grid-size pulses in the tropics, which is not necessarily realistic. The spectrum from the SKYHI-N45L80 model (not shown in Fig. 4) is similar to SKYHI-N30L45, but the total variance obtained by integrating the power is larger in the former than in the latter, since the former has a larger resolution and hence has an additional wavenumber range to contribute to the variance.

The overall power with the ZM scheme (MACCM3, CMAM, FVCCM) is the smallest (Figs. 4 and 5), although it is larger in CMAM than in the other two. The difference between the CMAM and the CCM models is discussed in Section 4 (although both use the ZM scheme, there is some difference between them in addition to the difference in resolution). The UKMO model also produces small power except for at high frequencies, where, interestingly, the spectra increases with frequency except for the harmonics of the diurnal frequency. In these four models (MACCM3, CMAM, FVCCM, and UKMO), the spectra have sharp peaks with respect to frequency at the diurnal frequency and its higher harmonics. The peaks have only small dependency on zonal wavenumber. Diurnal variations of convection are predominantly over continents. Except for these spikes with respect to frequency, the spectra are rather smooth and continuous, with maxima roughly around the period of 10 days. Westward-moving components are a little larger than eastward-moving components.

The overall power of precipitation in the MRI/JMA98 (with the prognostic AS scheme), FUB (Kuo scheme), and MAECHAM4 (Tiedtke scheme) models are in between the maximum (with the MCA scheme) and minimum (ZM and GR scheme) cases

mentioned above. In addition to spikes at the diurnal frequency and its harmonics, the precipitation in the MRI/JMA98 model shows a continuous peak around the period of 1 day, while in the FUB model a continuous peak is found around the period of 5 days. The overall power in the MAECHAM4 model is a little larger than that in the two models. It has a continuous peak around the period of 1 day, but the power is large over a quite broad range from 0.03 cpd to 4 cpd. The spectral shape looks like what would be obtained by adding the powers in the MRI/JMA98 and FUB models.

The large overall difference in the spectra among the models indicates that the variance of precipitation, which is obtained by integrating the spectra, is different as large as by more than one order of magnitude. However, the difference in the mean precipitation over the equatorial region is of course much smaller than it. These results indicate that the difference of variance is primarily due the difference in intermittency; the variance is small (large) if precipitation is continuous (intermittent) with time when the time-averaged precipitation is roughly constant. Therefore, the small variance with the ZH scheme, for example, should be because the modeled precipitation is less variable with time than that with the MCA scheme.

The middle and right panels in Fig. 4 shows zonal wavenumber-frequency distribution of the vertical component of the Eliassen-Palm (EP) flux averaged between 10N and 10S (the vertical component and its zonal wavenumber-frequency distribution are referred to as $F^{(z)}$ and $\tilde{F}^{(z)}$, respectively, hereinafter. The latter is defined by Eq.(A2)). Negative (positive) values indicate upward group propagation for waves that propagate eastward (westward) with respect to the mean flow, which is shown by the thick solid lines. To calculate $\tilde{F}^{(z)}$ near 1 hPa (right panels), the period of data used was limited to two months of December and January, since the mean zonal winds around the level change faster than those in the lower stratosphere because of the semiannual oscillation, which degrades the representativeness of $\bar{u}$ in Eq. (A2) if a long period is taken. The shaded region in each panel on the right-hand side of Fig. 4 indicates that there is a critical level between 100 hPa and 1 hPa for a wave whose wavenumber and frequency are in it.

At slightly above the tropopause (panels in the mid column in Fig. 4), the sign of $\tilde{F}^{(z)}$ is predominantly negative (positive) for eastward (westward) moving components, indicating the dominance of upward group propagation. Exceptionally, westward-moving semidiurnal tides with wavenumber up to 3 show downward group propagation in most models. It is probably because the vertical level is below the maximum ozone heating. Also, in some models, especially the MAECHAM4, the EP flux shows positive values for eastward moving, synoptic-scale, and slow phase-speed (less than 20 m/s) components. A separate examination clearly indicated that it is due to synoptic-scale Rossby waves from higher latitudes, whose group-propagation direction is predominantly equatorward and slightly upward (not shown).

Figure 6 shows frequency spectra similar to those in Fig. 5 but for temperature (T) and vertical pressure velocity (Dp/Dt) at around 65 hPa. In addition, the frequency distribution of $F^{(z)}$ is shown separately for eastward and westward moving disturbances. As expected, the spectra of temperature have larger negative slopes than those of vertical velocity. As a consequence, the slopes of the frequency distribution of $F^{(z)}$, which is dominated by the co-spectrum between zonal and vertical winds, are roughly between those of the spectra of the two. The spectra of zonal winds have similar shape to temperature spectra (not shown). Meridional-wind spectra are also similar (not shown), but because of the absence of Kelvin-wave signatures they are smaller than those of zonal wind at frequencies less than 0.2 cpd. It is noteworthy that $F^{(z)}$ in the CMAM is larger than would be expected from the spectra of precipitation in comparison with other models. This result indicates that wave excitation in this model is somehow more effective than in others. Since $|F^{(z)}|$ is large in both eastward and westward moving components, it is not explained by an effect of the mean flow. The vertical profile of diabatic heating could be useful to investigate the cause if the data were available. See Nissen et al. [2000] for an example of the impact of the vertical structure of diabatic heating.

Figure 6

As seen in Figs. 4 and 6, there is a large difference among the models with respect to the magnitude of $\tilde{F}^{(z)}$. It is obvious that it differs in a very similar way to the difference

in the power of precipitation. The correspondence between $\tilde{F}^{(z)}$ and precipitation spectra is surprisingly good, except, at around 65 hPa, for the signature of Rossby-waves from higher latitudes and, at around 1 hPa, for wavenumber-frequency ranges in which critical levels exist (shaded region). The good correspondence between the precipitation spectra and $\tilde{F}^{(z)}$ continues to higher altitudes in the mesosphere (not shown).

The difference of the power of precipitation is explained mainly by that of cumulus parameterization methods, as stated earlier. Therefore, we can conclude that choice of a cumulus parameterization profoundly affect the generation of vertically propagating waves in the models. Note, however, that the power of precipitation is not uniformly "projected" onto the vertically propagating waves, as shown by Salby and Garcia [1987]. For example, the EP flux is small for small zonal phase velocities unlike the power of precipitation. Also, there are a number of factors that affect wave propagation (see Section 1), but the fact that there is a clear correspondence between the precipitation spectra and $\tilde{F}^{(z)}$ throughout the middle atmosphere suggests the importance of convective parameterization.

3.3. Comparison with observations

In addition to the modeled spectra, Fig. 5 shows the spectra[1] of precipitation shown by RG2000 and Horinouchi [2002]. The spectra in RG2000 are estimated from global cloud imagery of infrared brightness temperature from geostationary satellites. It is averaged over the entire equatorial region between 15N and 15S. On the other hand, the spectra from Horinouchi [2002] are derived from regional data. These are derived from precipitation during the Tropical Oceans and Global Atmosphere Coupled Ocean-Atmosphere Response Experiment (TOGA-COARE) Intensive observation

[1]Since the spectrum shown in RG2000 was accidentally multiplied by a factor of 2 (Lucrezia Ricciardulli, personal communication), it is halved. Then it is multiplied by a factor to convert the units. The factor is 2.34×10^{-15} to convert K^2/day to m^2s^{-2}day [see Horinouchi, 2002].

period (IOP) conducted over the western Pacific. Among his two estimates, one is calculated from 3-hourly 2°-by-2°-average precipitation from dual ship-borne C-band radars. The other is estimated from satellite brightness temperature with the same method as used by RG2000 for the same period and area as the TOGA-COARE radar data (see Horinouchi [2002] for details).

For both TOGA-COARE and equatorial-mean cases, satellite precipitation in Fig. 5 was first derived from brightness temperature averaged over 0.25-degree^2 grid cells ($0.5° \times 0.5°$ for the former and $0.7° \times 0.35°$ for the latter). The estimated grid-mean precipitation was then averaged over multiple grid cells before deriving the spectra. The number of the cell are different for the two cases: for the TOGA-COARE case it is 16 cells in a 2° by 2° region, while for the other case it is equivalent to approximately 2 cells. The latter is because RG2000 truncated zonal wavenumber at about half of its maximum (120 out of 257) before integrating with wavenumber to get the frequency spectrum. The equatorial-region-mean spectrum is larger than the TOGA-COARE spectrum for frequencies higher than 1 cpd, but this is very likely due to the difference in the area of averaging. For the TOGA-COARE case, the 16-cell spectrum is lower than the one-cell spectrum (not shown) for such high frequencies by several times to one order, while the former is smaller than the latter only by a factor of 2 or so for frequencies between 0.1 and 0.3 cpd [Horinouchi, 2002]. It is, therefore, expected that the RG2000 spectrum is smaller if precipitation with the same resolution as the TOGA-COARE case (i.e., 4-degree^2) is used. It is likely smaller than the TOGA-COARE spectrum throughout the frequency range plotted, since the TOGA-COARE observation was conducted with relatively large convection activity.

From Fig. 5, it is obvious that the RG2000 method severely overestimates the spectrum compared with the radar observation for the TOGA-COARE case. It is because the intermittency of the precipitation over a 4-degree^2 scale is overestimated by the satellite-brightness temperature algorithm. If the RG2000 method overestimates the power spectrum of precipitation not only for the TOGA-COARE case but in general, as suggested by Horinouchi [2002], then the equatorial-region-mean spectrum on the

4-degree^2 scale should be much smaller than that presented by RG2000, and it may be below the TOGA-COARE radar-based spectrum shown in Fig. 5. The area of 2° by 2° is even smaller than that of grid cells of most models analyzed in the present study. It should be stressed that the variance of precipitation is expected mathematically to increase by decreasing the area over which to average. Therefore, the spectrum of the 4-degree^2-grid precipitation may be underestimate for sake of the comparison with the models even if the measurements are accurate.

If the spectra from the models are to be compared to the equatorial-region-mean RG2000 spectrum in Fig. 5, those spectra obtained in the models with the MCA scheme are slightly overestimated but closer to the observation than those with other schemes, which are underestimated. However, as stated above, the RG2000 spectrum is likely a severe overestimate. At this moment, no reliable estimate to cover the entire equatorial region is available. However, if it is assumed that the reality is close to the radar-based spectrum for the TOGA-COARE case, as mentioned above, then we may conclude that the spectra obtained with the MAECHAM4 model with the Tiedtke scheme or the MRI/JMA98 model with the prognostic AS scheme are more realistic than those with others; those with the MCA scheme are too large, and those with the ZM (CMAM and CCM) and the GR scheme (UKMO) are too small except for sharp tidal peaks. The above is perhaps the best argument one can do with the state-of-art knowledge on the equatorial precipitation. More observational studies are needed to evaluate the spectra with confidence.

Hertzog and Vial [2001] (HV01) derived spectra with respect to intrinsic frequency by using three "super-pressure" balloons, which float at roughly a constant pressure of 50 hPa. The spectral slopes they obtained for frequencies above 1 cpd are shallower than most of those shown in Fig. 6. Their results are about -2 for u and v, 0 for vertical wind for frequencies over 0.3 cpd, and -1 for both eastward and westward moving contributions to $F^{(z)}$ for frequencies between 1 and 0.04 cpd.

The magnitude of modeled $F^{(z)}$ at around 65 hPa is summarized in Table 4, which shows $|F^{(z)}| \equiv F_{\rm w}^{(z)} - F_{\rm e}^{(z)}$, where $F_{\rm w}^{(z)}$ and $F_{\rm e}^{(z)}$ represent decomposition of $F^{(z)}$ onto

contributions from westward- and eastward-moving disturbances, respectively. Also shown in the table are observational estimates taken from Sato and Dunkerton [1997] (SD97) and HV01. SD97 estimated $|F^{(z)}|$ from multi-year operational radiosonde observation at Singapore by using co-spectrum of u and T. They showed that $|F^{(z)}|$ due to disturbances with frequency between 0.33 and 1 cpd excluding tides was 0.01 $\sim$ 0.02 $\mathrm{m^2 s^{-2}}$ at around 65 hPa, which are equivalent to 0.65×10^{-3} and 1.3×10^{-3} J, respectively. They stated that the actual value could be 30 $\sim$ 70 % of their estimation, if some equatorial wave modes are considered as the carrier of momentum instead of pure internal gravity waves or Kelvin waves. Thus, for reference, we added in Table 4 their minimum case obtained by multiplying 0.3. Since their study is based on a observation at a single point, all scale of disturbances are included. However, gravity waves with frequencies less than 1 cpd are dominated by waves with horizontal wavelength larger than 1000 km, which are resolved in GCMs.

HV01 estimated $|F^{(z)}|$ with a different method. They derived w from the pressure sensors on the balloons and obtained $|\overline{u'w'}|$ along each balloon's trajectory approximately by using wavelet transform, where, before taking summation, they reverted the sign of each product of wavelet coefficients between u and w if it is negative. This calculation, however, is not mathematically equivalent to calculate $|\overline{u'w'}| \equiv \overline{u'w'}_{\mathrm{e}} - \overline{u'w'}_{\mathrm{w}}$ based on space-time Fourier transformation, and it could underestimate $|\overline{u'w'}|$. Therefore, care must be taken to compare their results with those by SD97 or from models. The average of their estimates of $|\overline{u'w'}|$ integrated over frequency from 1 to 24 cpd is 0.01 $\mathrm{m^2 s^{-2}}$. Since the spectral slope is roughly -1 with frequency, it is logarithmically equi-partition, which means that the integration between 1 and 3.3 cpd is approximated by multiplying $\log(3.3)/\log(24) = 0.38$. Therefore, the value in Table 4, 0.2×10^{-3} J, is obtained from $0.01 \times 0.38 \times (50/1000)$, where the last term is because of the pressure level of 50 hPa. Note that, if the spectral slope remains to be -1 below 1 cpd, the values corresponding to SD97 and HV01's estimates should be equal to each other. It is not the case in Table 4, unless the smallest estimate by SD97 is taken or HV01 underestimated the momentum flux (or the difference is within the natural variability, whether it is with

space or time).

As have been stated, there are large uncertainties in observational estimates. Nevertheless, it is worth making a comparison between the model results and available observational estimates. The results shown in Table 4 is not inconsistent with what was stated with Fig. 5, unless the maximum value of SD97's estimate should be used. Namely, convective excitation in the models with the MCA scheme is too strong and that in the models with the ZM and GR schemes is too weak.

3.4. Kelvin, gravity and tidal waves

We present in this section the relative contributions of different kinds of waves to energy and momentum flux in modeled equatorial middle atmospheres. It is done by separating waves spectrally in the zonal wavenumber-frequency domain.

Figure 7 shows the kinetic energy of disturbances of selected wavenumber-frequency ranges. Thick dashed lines show that of eastward-moving low-frequency (up to 0.3 cpd), low-wavenumber (1 to 3) disturbances, which include planetary-scale Kelvin waves. In the MACCM3 (and similarly in the FVCCM, though not shown), the energy associated with these disturbances are more than half of the kinetic energy of the whole eastward-moving disturbances in the stratosphere. The ratio is smaller in the other models, but it is larger than one-third in many cases. Also, the ratio is smaller in the mesosphere than in the stratosphere for all the models. Contrary to the statistics of kinetic energy, the contribution of these low-wavenumber, low-frequency disturbances is much smaller in $F^{(z)}$ than in the kinetic energy, as shown in Fig. 8. For most altitudes, it is 10 % or less in models other than MACCM3 and FVCCM, in which the ratio is about half or less. Therefore, the momentum transfer due to Kelvin waves are far from dominant in most models. The contrast between the ratio in terms of kinetic energy and the EP flux is explained by the contribution of the vertical wind, whose spectra are shallower with respect to both frequency and zonal wavenumber than those of horizontal winds. Therefore, the ratio of the contribution from high wavenumber/frequency waves in $F^{(z)}$ is larger than that in kinetic energy.

Figure 7

Fig. 8

As indicated by the two-dimensional spectra of precipitation and momentum flux (Fig. 4), there is a clear overall correspondence between the $F^{(z)}$ due to non-migrating diurnal tides and the power of diurnal components of precipitation. The result indicates that a significant fraction of the non-migrating tides in the equatorial stratosphere is due to convective heating in the models, as suggested by previous studies [Hamilton, 1981; Tokioka and Yagai, 1987; Lieberman and Leovy, 1995; Williams and Avery, 1996]. Figure 7 shows that in all models the kinetic energy of eastward-moving non-migrating tides (thin dashed lines) are smaller than that of the low-frequency, low-wavenumber disturbances including Kelvin waves (thick dashed lines) in the stratosphere. The energy of the former is relatively large in the mesosphere, and in some models it is larger than the energy of the latter at around 0.01 hPa. On the other hand, as seen in Fig. 8, $F^{(z)}$ associated with the non-migrating tides is larger than that of the low-frequency, low-wavenumber disturbances throughout the upper stratosphere and mesosphere in most models. Therefore, the momentum transport by the eastward-moving non-migrating tides is larger than that by planetary-scale Kelvin waves above the lower stratosphere in most models. Nonetheless, the summation of $F^{(z)}$ attributed to these waves (the non-migrating tides and planetary-scale Kelvin waves) explains only a small portion of the total $F^{(z)}$ due to eastward-moving disturbances except for FVCCM and CMAM. The remaining is mostly attributed to non-tidal gravity waves.

A large portion of westward-moving gravity waves, on the other hand, encounter the critical levels before reaching the stratopause due to the solsticial easterly wind as shown in Fig. 4. Therefore, it is not surprising that tides carry a significant portion of $F^{(z)}$ due to westward-moving disturbances above upper stratosphere in many models (Fig. 8). The sign of $F^{(z)}$ due to the migrating diurnal tide is positive in general, which indicates upward energy propagation, but it is negative below the stratopause where the ozone heating maximizes (negative values are not plotted because of the logarithmic scaling). It is also negative, or positive but minimum, at levels around 0.2 hPa. In most models $F^{(z)}$ associated with the migrating diurnal tide around this level is upward in the vicinity of the equator, but is equatorward and slightly downward in the tropics off the

equator (not shown). Unlike that due to migrating tides, $F^{(z)}$ due to non-migrating tides (dotted lines) decreases roughly monotonically with altitude in most models, indicating excitation in the troposphere. Its magnitude is smaller than that due to migrating tides above 0.1 hPa. In the lower stratosphere, however, a large-portion of $F^(z)$ is attributed to westward-moving non-migrating tides in most models.

In many models, kinetic energy of westward-moving non-migrating tides (dotted lines in Fig. 7) are comparable to or even larger than that of the migrating tides (dash-dotted lines) for a large range of altitudes. In most models the energy is broadly distributed from $s = -2$ to $s = -10$ in the stratosphere (not shown). In the mesosphere the energy is explained mostly by waves with $s = -2$ to -4, except for CMAM and MACCM3, in which non-migrating tides of $s < -4$ retain energy comparable to that of tides with $s = -2$ to -4 (not shown). Hagan et al. [1997] estimated the amplitude of non-migrating tides excited by convective heating using satellite-observed brightness temperature data with a method similar to that by RG2000. They showed that the kinetic energy, which is measured by $u^2 + v^2$ here, of westward-nonmigrating tides of $s = -2$ (westward) are roughly 2 m^2s^{-2} at 0.1 hPa. Among the models analyzed in this paper, MRI/JMA98, FUB, MACCM3, and CMAM have the $s = -2$ tide with comparable or a little larger amplitude at this level, while it is about 10 m^2s^{-2} in ECHAM and UKMO, and 0.1 m^2s^{-2} in FVCCM (not shown).

Unlike $F^{(z)}$, however, the energy of the whole westward-moving tides explains only a small portion for the kinetic energy of the whole westward-moving disturbances in all models. A separate investigation revealed (not shown) that the kinetic energy in the stratosphere is dominated by planetary-scale disturbances with frequencies less than 0.2 cpd, which indicates the dominance of Rossby waves. The contribution from higher frequency gravity waves increase with altitude, and they are dominant in the mesosphere in most cases. Typically, both Rossby and gravity waves contribute significantly to the kinetic energy around the stratopause.

The partitioning of $F^{(z)}$ among various waves is further examined with Fig. 9 and 10, which show the wavenumber distribution of $F^{(z)}$ for various frequency ranges at

Fig. 9 and

around 65 and 1 hPa. Disturbances with ω between 0.1 and 0.3 cpd (upper-left panels) have slow phase speeds except for those with low wavenumbers (see the dotted lines in Fig. 4 to see the correspondence among s, ω, and zonal phase speed). Thus, they are susceptible to critical level absorption, as is evident for westward-moving disturbances. The $s = +1$ component in this frequency range include the classical Kelvin waves with period from 10 to 20 days observed dominantly in the lower stratosphere and the "fast" and "ultra-fast" Kelvin waves which are observed in the upper stratosphere and mesosphere [Hirota, 1978; Salby et al., 1984]. From Figs. 9 and 10, it is clear that all of these waves carry only a very small fraction of momentum flux in all models.

Disturbances with ω between 0.3 and 0.97 cpd (upper-right panels) consists mostly of gravity waves including synoptic-scale Kelvin waves. In many models, eastward-moving components have spectral slopes roughly close to -1 between $s = 5$ and 20 at both levels. The slope of -1 indicates an equal partitioning along (logarithmically-scaled) wavenumber. The slope is similar for westward-moving components in the lower stratosphere (Fig. 9), but wave elimination due to the mean easterly winds distorts it around the stratopause (Fig. 10).

The diurnal tidal component of $F^{(z)}$ has sharp peaks at westward $s = -5$ and eastward $s = +3$ at 65 hPa (lower-left panel of Fig. 9) in most models that have the solar diurnal cycle. The result is consistent with the results by Williams and Avery [1996] that the diurnal convective heating derived from satellite cloud imagery peak at these wavenumbers. As in their case, it is explained by the land-sea distribution having a significant wavenumber-4 component. Namely, diurnal $s = -5$ and $s = +3$ components are obtained by the composition of a diurnal $s = -1$ component and a stationary $s = 4$ component [Tokioka and Yagai, 1987]. The diurnal signal of cumulus convection in the models are distributed predominantly over the African and South-American continents, and partly over the Maritime continent. The former two are separated roughly by 90°, which corresponds to $s = 4$. In the FUB model the $s = +3$ peak does not exist and the peak at $s = -5$ is weak. It is probably because the precipitation over the South America in this model is weak (see Fig. 2). The $s = +3$ peak is also absent in the MAECHAM4

model.

The $s = -5$ peaks in $F^{(z)}$ are largest among the non-migrating diurnal tidal components and are comparable to the the peaks at the migrating $s = -1$ component at 65 hPa. However, the $s = -5$ peaks are not significant at 1 hPa shown in the lower-left panel of Fig. 10, which is consistent with the results by Hagan et al. [1997]. On the other hand, the eastward-moving nonmigrating tides are still significant at this level.

Disturbances with frequencies larger than 1.03 cpd shown in the lower-right panels of Figs. 9 and 10 consists mostly of gravity waves including semi-diurnal and higher-frequency tides. The most of the momentum flux at 65 hPa (Fig. 9) are carried by waves with wavenumbers higher than 10. High wavenumber components are especially significant in the MAECHAM4, AGCM5, and SKYHI models, in which total $F^{(z)}$ is larger than in the other models.

3.5. Driving force of the SAO

It has been revealed that the momentum deposition by planetary-scale Kelvin waves is not sufficient to drive the westerly phase of the SAO, which suggests the importance of gravity waves of smaller scales (see Section 1). However, it is uncertain whether the Kelvin waves play a significant role in the driving or not. It is also uncertain whether which of gravity waves of synoptic to intermediate scales or those of mesoscale are important. Therefore, it is interesting to see how the momentum deposition is partitioned among various scales of waves in the driving force of the SAO in the models. Among the models analyzed, MAECHAM4, MACCM3, and UKMO models have parameterizations of non-stationary gravity waves. Therefore, the forcing of the SAO in these model can come from parameterized gravity waves as well as resolved waves, while in the other models the eddy forcing of the SAO is solely due to resolved waves.

Figure 11 shows contributions from various wavenumber-frequency ranges of disturbances to the EP flux divergence over the latter half of the DJF period (i.e., the latter half of January and the whole February). In this period of year, westerly winds appear in the lower mesosphere and descends gradually to the upper stratosphere [e.g.,

Garcia et al., 1997]. The observed tendency of zonal mean wind of the period is about 1 m/s/day at the altitude of maximum tendency. However, because of the easterly acceleration due to the meridional circulation, the westerly eddy momentum deposition required is much larger than this value and may be as large as 4 m/s/day, as seen in the simulation by Sassi and Garcia [1997].

The EP flux divergence in a half of the models (FUB, MAECHAM4, CMAM, SKYHI-N30L40) shows positive peaks around 4 m/s/day or larger in the lower mesosphere (thin solid lines in Fig. 11). However, planetary-scale Kelvin waves contribute only small fractions in all of them (thick-dashed lines). Especially, the contribution of $s = 1$ Kelvin waves is negligible (thin-dashed lines). From these results, it is understood why Amodei et al. [2001], who analyzed $s = 1$ Kelvin waves and the SAO in some GCMs, did not find a relation between them.

The waves contributing most to the westerly acceleration in the lower mesosphere are different among the four models. In the FUB model, disturbances with $s \geq 4$ and $\omega < 0.97$ dominate it, with a secondary contribution from disturbances with $1 \leq s \leq 3$ and $\omega < 0.3$. The former consists of gravity waves and synoptic-or-smaller-scale Kelvin waves, while the latter include planetary-scale Kelvin waves. In the other three models, there are significant contributions from disturbances with diurnal or higher frequencies as well as those with sub-diurnal frequencies. The difference between the FUB and other models is consistent with that in the frequency distribution of $F^{(z)}$ at the stratopause level as seen in Fig. 4, which is due to the difference in the precipitation spectra in Fig. 4. In the CMAM, contribution from eastward-moving nonmigrating tides (thick dotted line) is second largest, while in the MAECHAM4 model it is minor and comparable to that from disturbances with $1 \leq s \leq 3$ and $\omega < 0.3$.

The SAO in the FUB model was investigated by Müller et al. [1997]. Although the period and altitude used to study the momentum budget is different (they used data in March and calculated momentum budget at the stratopause level), the result obtained here is consistent with their result. Namely, the westerly acceleration of the SAO is dominated by waves with $\omega > 0.3$ cpd, and the role of planetary-scale Kelvin waves

in it is minor. They estimated that the contribution of the Kelvin waves identified subjectively was 18 % in the acceleration. Even this ratio may be higher than a typical value for the SAO in GCMs, given the difference among models mentioned above. The result for the SAO in the SKYHI-N30L40 model is consistent with those presented by Hamilton and Mahlman [1988] who used the SKYHI with the same resolution (see Section 1).

The EP flux divergence in the MACCM3, FVCCM, and UKMO models does not show positive values in the lower mesosphere. This result suggests that the SAO in the MACCM3 and UKMO models are driven mainly by parameterized non-stationary gravity waves. The MAECHAM4 models also have such a parameterization. Therefore, the SAO in them is assisted by parameterized gravity-wave drag.

The EP flux divergence in the MRI/JMA98 model has a peak of a similar magnitude to that in the four models discussed earlier (FUB, MAECHAM4, CMAM, and SKYHI-N30L40), but the peak is in the upper mesosphere. The SAO in this model is very week (Fig. 1). From comparison with the FUB model, it appears that the reason why the MRI/JMA98 model has only a very weak SAO is partly that the $\tilde{F}^{(z)}$ is weak for frequencies lower than 1 cpd.

The results of this study is consistent with those which suggested that the role of planetary-scale Kelvin waves is minor in the SAO (see Section 1). In all the models their role is fairly small. Note that the wave forcing in the numerical experiment by Sassi and Garcia [1997], in which a realistic SAO is reproduced with some significant contribution from planetary-scale Kelvin waves, is "guided" by observation in an ad hoc way. The relative importance of resolved and unresolved waves in the SAO driving is different among models, and it is difficult to tell which is realistic.

4. Discussion

We discuss in this section the cumulus parameterizations used in the models investigated in terms of wave excitation. Table 5 summarizes the parameterizations. Most of them are mass flux schemes initiated by Arakawa and Shubert [1974], most

Table 5

of whose closure are based on convective available potential energy (CAPE). The AS scheme uses the cloud work function (CWF) instead of CAPE, but it is interpreted as a generalized CAPE. Exceptionally, the GR scheme in the UKMO model uses the buoyancy of a parcel at one level above the cloud base in which the parcel is originated. In most of the CAPE- (or CWF-) based mass flux schemes (ZM and AS schemes) deep convection is initiated, or "triggered", if CAPE or CWF is positive so as to realize the quasi-equilibrium. The Tiedtke scheme is originally closed by moisture supply on the resolved scale [Tiedtke, 1989], as in the Kuo scheme. In the MAECHAM4 model, it is modified by Nordeng [1994] to use CAPE for its closure. However, it still uses the moisture supply to determine the possibility of having the deep convection.

All of the mass flux schemes examined here have parameterized convective downdraft. Some of the schemes include parameterizations of shallow- or midlevel-convection (see the table). The ZM scheme supports only deep convection, but the CCM3 applies the Hack scheme after the ZM scheme to cover midlevel convection, while the CMAM does not. All the models have large-scale condensation, which removes grid-scale super saturation.

As have been shown above as well as by RG2000, the temporal variability of cumulus convection produced by the ZM scheme is fairly small. Guang and Guo [2001] attributed the reason for this to the lack of a mechanism to inhibit convection (deep convection is initiated whenever CAPE is positive). The result that the Tiedtke scheme produced a large variability can be understood in this line; although the MAECHAM4 version of the Tiedtke scheme is closed in terms of CAPE, large-scale moisture supply is needed to initiate deep convection. It is also interesting that the shape of the precipitation spectrum in MAECHAM4 shown in Fig. 4 is somewhat similar to that with the Kuo scheme (FUB), which is closed with the moisture supply. The AS scheme in the MRI/JMA98 model is closed prognostically, where the CWF is relaxed to zero. Although the effect of the prognostic closure on the simulated precipitation variability is not clear here, it is probably not large, since the relaxation time scale is set to be small enough to mimic the quasi equilibrium condition introduced by Arakawa and Shubert

[1974]. Then, it is not clear why the AS scheme produced a little larger variability than the ZM scheme. It is also noteworthy that the continuous peak with frequency is around 0.1 cpd with the ZM scheme, while it is around 1 cpd with the prognostic AS scheme. These differences of the two schemes are probably due to the difference in details of the cloud models they assume. For instance, Maloney and Hartmann [2001] suggested the impact of the treatment of convective downdraft on the simulation of Madden-Julian oscillation.

Although both CMAM and CCM3 (MACCM and FVCCM) use the ZM scheme, the variability of precipitation is larger in the latter model than in the former. The difference might be because only the CCM3 has a parameterization of midlevel convection. Also, there is a difference in the value of tunable parameter between the two models (John Scinocca, personal communication); the CAPE relaxation time is set to be 2400 sec in the former, while it is 7200 sec in the latter. The effects of these factors are currently under investigation. In the UKMO model with the GR scheme, power of precipitation is as small as that produced by the ZR scheme except for high frequencies greater than 1.5 cpd. Gregory and Rowntree [1990] wrote that, although the closure of the scheme is not directly related to the quasi-equilibrium, the scheme tends to realize it, though not on the time-step by time-step basis. Therefore, the high-frequency enhancement and the small power at low-frequency may be a consequence of the closure.

The MCA scheme has a tunable parameter on the relative humidity toward which the adjustment is conducted. The original formulation by Manabe et al [1965] corresponds to set the parameter, say γ, equal to 1 (100 %). By using a single-column test with forcing taken from observational soundings, Krishnamurti et al. [1980] showed that the MCA scheme with $\gamma = 1$ produced too large precipitation. The precipitation matched most to the observation when $\gamma = 0.82$, with which the overall amount of rainfall is roughly realistic but the time sequence of precipitation was still poorly reproduced. In their simulations, the Kuo scheme with similar configuration to that used in the current FUB model reproduced observational precipitation much better than the MCA with $\gamma = 0.82$, but there is not an apparent difference in the variance of

precipitation inferred from their figures. The values of γ used in the two models with the MCA scheme is 0.85 in the SKYHI models and 0.99 in the AGCM5. Contrary to the single-column results, even the SKYHI produce the variability of precipitation much larger than that in the FUB model, while the difference between SKYHI and AGCM5 is small. The result indicates a limitation of single-column experiments in which cumulus convection does not interact with large-scale dynamics.

5. Conclusions

Resolved waves in the equatorial middle atmosphere of various GCMs were investigated in this study by using space-time Fourier analyses. Precipitation was examined as a proxy to the diabatic forcing of the waves. It was revealed that overall variability of precipitation differs by more than one order of magnitude among models. The spectral shapes also have a large difference. The difference can mostly be explained by the use of different convective parameterizations. The classical MCA scheme used in the SKYHI and AGCM5 models produces the largest variability, while the ZM and GR schemes produces the smallest variability, although both produce significant diurnal cycle in the precipitation over land. In addition to sharp peaks at the diurnal frequency and its higher harmonics, each cumulus parameterization produces broad spectral peaks at different frequencies (for instance at around 0.1 cpd with the ZM scheme)

The fluctuating component of the cumulus convection dominate the generation of the resolved waves that propagate in the equatorial middle atmosphere of the GCMs. A remarkable correspondence was found between the space-time spectra of precipitation and the wavenumber-frequency distribution of the vertical component of the EP flux in the lower stratosphere for each model. The correspondence is clear even throughout the middle atmosphere except for waves that experience critical levels at lower altitudes. Since the spectra of precipitation are dominated by cumulus parameterization, we can conclude that the choice of cumulus parameterization has a profound impact on the vertically propagating waves in the equatorial middle atmosphere. However, there are other factors that are important, especially for the propagation of the waves, as has

been shown in past studies. For instance, vertical resolution is important both directly through its capability of resolving waves [Boville and Randel, 1992] and indirectly by modifying environmental conditions [Nissen et al., 2000]. Also, a change in what does not seem to be significant for wave propagation, such as radiation, may alter a background condition, and that can be amplified through wave-mean flow interaction, leading to a major difference in climatology as indicated by simulations by Nissen et al. [2000] and Giorgetta et al. [2002]. Giorgetta et al. [2002] obtained a realistic QBO-like oscillation in the MAECHAM5 model but not in the MAECHAM4 model, both of which use the same cumulus parameterization.

Frequency spectra of precipitation in the models were compared with "observations". Those with the MCA scheme compares best to the satellite-derived spectrum by RG2000, but the RG2000 spectrum is likely an overestimate. Furthermore, the horizontal resolution of the precipitation data to compute it is too high to compare with GCM results, which increases power. Therefore, the actual spectrum to compare should be much lower than it. From the comparison with the TOGA-COARE case, the spectra obtained with the MAECHAM4 and MRI/JMA98 models are likely more realistic. We also made a comparison with currently available observational estimates of $F^{(z)}$. Although there is a large uncertainty in observational estimate, it is also suggested that observational $F^{(z)}$ due to waves with scales resolvable in GCMs are probably somewhere in the middle of the wide variety of their simulated values.

Given that only models with the MCA cumulus parameterization, which produced highest precipitation variability, have simulated the QBO without gravity wave parameterization, the QBO in the atmosphere probably owes its forcing partly to subgrid- (or meso-) scale gravity waves. It is indicative that Giorgetta et al. [2002] showed that the MAECHAM5 model, which uses the same cumulus parameterization as the MAECHAM4 investigated here, simulated a realistic QBO, where it is driven roughly equally by resolved and parameterized waves.

In most models, eastward-moving disturbances with $s \leq 3$ and $\omega < 0.3$, which include Kelvin waves, accounts for one-third to half of the total kinetic energy of

eastward-moving disturbances in the stratosphere. As for the vertical component of the EP flux, however, the contribution of these disturbances is generally less than 10 %. Parameterized cumulus convection excites non-migrating tides with broad range of zonal wavenumber, which should predominantly be gravity waves. Although the kinetic energy associated with non-migrating tides account for only a small fraction of the total kinetic energy, the momentum flux associated with them is not negligible. In most models, the flux associated with eastward-moving nonmigrating tides is larger than that associated with planetary-scale Kelvin waves above 10 hPa, whose possibility has not been argued in literature. In terms of momentum transport, however, the most significant are non-tidal gravity waves in most models. These waves are also the biggest contributer to kinetic energy in the mesosphere.

The waves contributing to the driving of the simulated SAO are found to differ among models. However, in all models the role of planetary-scale Kelvin waves is fairly small. Especially, the contribution of the $s = 1$ ultra-fast Kelvin wave is negligible. In most models, the SAO is driven mainly by gravity waves with periods less than 3 days (especially less than 1 day in many cases) and/or parameterized non-stationary gravity waves.

We could successfully quantify resolved waves in various middle atmospheric GCMs in terms mainly of momentum flux. However, the comparison with observations are not thorough because of the limited coverage of observation and the difficulty in measuring vertical winds. More observations are needed to further assess the GCMs to improve them with physical bases. For this purpose, it is probably needed to develop new satellite algorithms. Also important may be vertical wind observations by high-powered radars.

Appendix: Spectral calculation

All the spectra shown in this paper is first calculated two-dimensionally with respect to zonal wavenumber s and frequency ω by using the fast Fourier transform after subtracting mean values and applying a tapering with respect to time. They

are one-sided with frequency so that a power spectrum $P(s,\omega)$ of a quantity $q(\lambda,t)$ is normalized to satisfy

$$\frac{1}{2\pi T}\int_0^{2\pi}\int_{t_0}^{t_0+T}|q^2|\,dtd\lambda = \sum_{s=-N/2}^{N/2}\sum_{j=0}^{j_{\max}}P(s,\omega_j)\Delta\omega, \tag{A1}$$

where $\Delta\omega \equiv 1/T$ (in cpd), and N is the number of grid points with longitude. When the spectrum is shown in the energy-content form, it is multiplied with s and ω, so its units becomes equal to that of $|q^2|$.

The zonal wavenumber-frequency distribution of the vertical component of the EP flux, $\tilde{F}^{(z)}$, is calculated from cross spectra as:

$$\begin{aligned}\tilde{F}^{(z)}(s,\omega) &\equiv (p/p_0)\cos(\phi)\,\mathrm{Re}[\,Zc\hat{v}(s,\omega)\hat{\theta}^*(s,\omega)\\ &\quad - c\hat{u}(s,\omega)\hat{w}^*(s,\omega)\,],\\ Z &\equiv \left[f-(a\cos\phi)^{-1}(\bar{u}\cos\phi)_\phi\right]\bar{\theta}_z{}^{-1}.\end{aligned} \tag{A2}$$

Here, asterisk expresses complex conjugate, $\hat{u}$, $\hat{v}$, $\hat{w}$, and $\hat{\theta}$ are the Fourier coefficients of zonal, meridional and vertical winds, and potential temperature, respectively, and c is a constant to convert multiples of Fourier coefficients to power spectra. The mean potential temperature $\bar{\theta}$ and zonal wind $\bar{u}$ are obtained by zonally and temporally averaging θ and u over the period used for the spectral calculation, and the reference pressure p_0 is 1000 hPa. Other symbols are in the standard notation (see Andrews et al.[1987]).

For line and two-dimensional plotting, spectra were smoothed by applying several passages of a 1-2-1 smoothing filter. The number of passage is greater for larger wavenumber/frequency. The filtering is only for a better display, so it is not applied, for example, with frequency when the spectra were divided in terms of frequency ranges as in Figs. 9 and 10.

Acknowledgments. The authors wish to thank Drs. Lucrezia Ricciardulli for providing the data of diabatic heating spectra, and John Scinocca and Charles McLandress for comments and discussion. TH is supported by the JSPS grant-in-aid 13740278.

References

Alexander, M.J., J. R. Holton, and D. R. Durran, 1995: The gravity-wave response above deep convection in a squall line simulation, *J. Atmos. Sci.*, **52**, 2212-2226.

Amodei, M., S. Pawson, A. A. Scaife, U. Langematz, W. Lahoz, D. M. Li, and P. Simon, 2001: The SAO and Kelvin waves in the EuroGRIPS GCMS and the UK Met. Office analyses, *Annales Geophysicae*, **19**, 99-114.

Andrews, D.G., J.R. Holton, and C.B. Leovy, 1987: *Middle Atmosphere Dynamics,* Academic Press, 489pp.

Arakawa, A., and W. H. Shubert, 1974: Interaction of a cumulus ensemble with the large-scale environment, Part I, *J. Atmos. Sci.*, **31**, 674-701.

Arakawa, A., and V. R. Lamb, 1977: Computational design of the basic dynamical processes of the UCLA General Circulation Model, *Methods in Computational Physics*, **17**, Academic Press, 174-265, 337pp.

Baldwin, M.P., L.J. Gray, T.J. Dunkerton, K. Hamilton, P.H. Haynes, W.J. Randel, J.R. Holton, M.J. Alexander, I. Hirota, T. Horinouchi, D.B.A. Jones, J.S. Kinnersley, C. Marquardt, K. Sato, and M. Takahashi, 2000: The Quasi-Biennial Oscillation, *Rev. of Geophys.*, **39**, 179-229.

Beagley, S. R., J. de Grandpre, J. N. Koshyk, N. A. McFarlane, and T. G. Shepherd, 1997 Radiative-dynamical climatology of the first-generation Canadian Middle Atmosphere Model, *Atmosphere-Ocean*, **35**, 293-331.

Bergman, J. W., and M. L. Salby, 1994: Equatorial wave activity derived from fluctuations in observed convection. *J. Atmos. Sci.*, **51**, 3791-3806.

Boville, B. A., and Randel, W. J., 1992: Equatorial waves in a stratospheric GCM: effects of vertical resolution. *J. Atmos. Sci.*, **49**, 785-801.

Cullen, M.J.P., 1993: The unified forecast climate model, *Meteorological Magazine*, **122**, 81-94.

Dunkerton, T.J., 1991: Nonlinear propagation of zonal winds in an atmosphere with Newtonian cooling and equatorial wave driving, *J. Atmos. Sci.*, **48**, 236-263.

Dunkerton, T.J., 1997: The role of gravity waves in the quasi-biennial oscillation, *J. Geophys. Res.*, **102**, 26,053-076.

Fujiwara, M., K. Kita, and T. Ogawa, 1998: Stratosphere-troposphere exchange of ozone associated with the equatorial Kelvin wave as observed with ozonesondes and

rawinsondes, *J. Geophys. Res.*, **103**, 19,173-182.

Garcia, R. R., T. J. Dunkerton, R. S. Lieberman, and R. A. Vincent, 1997: Climatology of the semiannual oscillation of the tropical middle atmosphere, *J. Geophys. Res.*, **102**, 26,019-032.

Giorgetta, M. A., E. Manzini, E. Roeckner, 2002: Forcing of the quasi-biennial oscillation from a broad spectrum of atmospheric waves, *Geophys. Res. Lett.*, **29**, 10.1029/2002GL014756.

Gregory, D., and P. R. Rowntree, 1990: A mass flux convection scheme with representation of cloud ensemble characteristics and stability-dependent closure, *Mon. Weather Rev.*, **118**, 1483-1506.

Guang, J.-Z., and M.-M. Guo, 2001: Preliminary evaluation of a revised Zhang-McFarlane convection scheme using the NCAR CCM3 GCM, *Advances in Atmospheric Sciences*, **18**, 710-717.

Hack, J, J., 1994: Parameterization of moist convection in the National Center for Atmospheric Research Community Climate Model (CCM2), *J. Geophys. Res.*, **99**, 5551-5568.

Hagan, M.E., J. L. Chang, and S. K. Avery, 1997: Global-scale wave model estimates of nonmigrating tidal effects, *J. Geophys. Res.*, **102**, 16,439-452.

Haltiner, G. J., and R. T. Williams, 1980: *Numerical Prediction and Dynamics Meteorology*, **Wiley**, 477 pp.

Hamilton, K., 1981: Latent heat release as a possible forcing mechanism for atmospheric tides, *Mon. Weather Rev.*, **109**, 3-17.

Hamilton, K., and J. D. Mahlman, 1988: General circulation model simulation of the semiannual oscillation of the tropical middle atmosphere, *J. Atmos. Sci.*, **45**, 3212-3235.

Hamilton, K., R. J. Wilson, J. D. Mahlman, and L. J. Umscheid, 1995: Climatology of the SKYHI troposphere-stratosphere-mesosphere general-circulation model, *J. Atmos. Sci.*, **52**, 5-43.

Hamilton, K., R. J. Wilson, and R. S. Hemler, 2001: Spontaneous stratospheric QBO-like oscillations simulated by the GFDL SKYHI general circulation model, *J. Atmos. Sci.*, **58**, 3271-3292.

Hayashi, Y., 1976: Non-singular response of equatorial waves under the radiation condition, *J. Atmos. Sci.*, , **33**, 183-201.

Hertzog, A., and F. Vial, 2001: A study of the dynamics of the equatorial lower stratosphere by

use of ultra-long-duration balloons 2. Gravity waves, *J. Geophys. Res.*, **106**, 22,745-761.

Hines, C.O., 1997a: Doppler-spread parameterization of gravity-wave momentum deposition in the middle atmosphere. 1.Basic formulation *J. Atmos. Solar-Terr. Phys*, **59**, 371-386.

Hines, C.O., 1997b: Doppler-spread parameterization of gravity-wave momentum deposition in the middle atmosphere. 2. Broad and quasi monochromatic spectra, and implementation, *J. Atmos. Solar-Terr. Phys*, **59**, 387-400.

Hirota, I., 1978: Equatorial waves in the upper stratosphere and mesosphere in relation to the semiannual oscillation of the zonal wind, *J. Atmos. Sci.*, **39**, 714-722.

Hitchman, M. H., and C. B. Leovy, 1988: Estimation of Kelvin wave contribution to the Semiannual Oscillation, *J. Atmos. Sci.*, **45**, 1462-1475.

Holton, J.R., and R.S. Lindzen, 1972: An updated theory for the quasi-biennial cycle of the tropical stratosphere. *J. Atmos. Sci.*, **29**, 1076-1080.

Holton, J. R., 1975: *The Dynamic Meteorology of the Stratosphere and Mesosphere, Meteorol. Monogr., 37*, **15**, No. 37, *Am. Meteorol. Soc.*, 216pp.

Holton, J.R., and W. M. Wehrbein, 1980: A numerical-model of the zonal mean circulation of the middle atmosphere, *Pageoph*, **118**, 284-306.

Holton, J.R., and H. C. Tan, 1980: The influence of the equatorial Quasi-Biennial Oscillation on the global circulation at 50 mb, *J. Atmos. Sci.*, **37**, 2200-2208.

Horinouchi, T., 2002: Mesoscale variability of tropical precipitation: validation of satellite estimates of wave forcing using TOGA-COARE radar data, *J. Atmos. Sci.*, **59**, 2428-2437.

Horinouchi, T. and S. Yoden, 1996: Excitation of transient waves by localized episodic heating in the tropics and their propagation into the middle atmosphere, *J. Meteor. Soc. Japan*, **74**, 189-210.

Horinouchi, T. and S. Yoden, 1998: Wave-mean flow interaction associated with a QBO-like oscillation simulated in a simplified GCM, *J. Atmos. Sci.*, **55**, 502-526.

Huffman G. J., R. F. Adler, P. Arkin, A. Chang, R. Ferraro, A. Gruber, J. Janowiak, A. McNab, B. Rudolf, and U. Schneider, 1997: The Global Precipitation Climatology Project (GPCP) combined precipitation dataset, *Bull. Am. Meteorol. Soc.*, **78**, 5–20.

Itoh, H., The response of equatorial waves to thermal forcing, 1977: *J. Meteor. Soc. Japan*, , **55**, 222-239.

Kiehl, J. T., J. J. Hack, G. B. Bonan, B. A. Boville, D. L. Williamson, and P. J. Rasch, 1998: The National Center for Atmospheric Research Community Climate Model: CCM3, *J. Clim.*, **11**, 1131-1149.

Krishnamurti, T. N., Y. Ramanathan, H.-L. Pan, R. J. Pasch, and J. Morinari, 1980: Cumulus Parameterization and rainfall rates I, *Mon. Weather Rev.*, **108**, 465-472.

Kuo H. L., 1974: Further studies of the parameterization of the influence of cumulus convection on the large scale flow, *J. Atmos. Sci.*, **31**, 1232-1240.

Langematz, U., 2000: An estimate of the impact of observed ozone loss on stratospheric temperature, *Geophys. Res. Lett.*, **27**, 2077-2080.

Lieberman, R. S, and C. B. Leovy, 1995: A numerical model of nonmigrating diurnal tides between the surface an 65 km, *J. Atmos. Sci.*, **52**, 389-409.

Lin, S.J., and R. B. Rood, 1996: Multidimensional flux-form semi-Lagrangian transport schemes, *Mon. Weather Rev.*, **124**, 2046-2070.

Lindzen, R. S., 1978: Effect of daily variations in cumulonimbus activity on the atmospheric semidiurnal tide. *Mon. Weather Rev.*, **106**, 526-533.

Lindzen, R. S., 1981: Turbulence and stress owing to gravity wave and tidal breakdown, *J. Geophys. Res.*, **86**, 9707-9714.

Lindzen R.S., and J.R. Holton, 1968: A theory of the quasi-biennial oscillation. *J. Atmos. Sci.*, **25**, 1095-1107.

Lindzen, R.S., and C.-Y. Tsay, 1975: Wave structure of the tropical stratosphere over the Marshall islands area during 1 April–1 July 1958. *J. Atmos. Sci.*, **32**, 2008–021.

Maloney, E. D., and D. L. Hartmann, 2001: The sensitivity of intraseasonal variability in the NCAR CCM3 to changes in convective parameterization, *J. Clim.*, **14**, 2015-2034.

McFarlane, N. A., 1987: Effect of orographically excited gravity wave drag on the general circulation of the lower stratosphere and troposphere, *J. Atmos. Sci.*, **44**, 1775-1800.

Manabe, S., J. Smagorinsky, R. F. Strickler, 1965: Simulated climatology of a general circulation model with a hydrological cycle, *Mon. Weather Rev.*, **93**, 769-798.

Manzini, E. and K. Hamilton, 1993: Middle atmospheric traveling waves forced by latent and convective heating. *J. Atmos. Sci.*, , **50**, 2180–2200.

Manzini, E., N. A. McFarlane, and C. McLandress, 1997: Impact of the Doppler spread parameterization on the simulation of the middle atmosphere circulation using the

MAECHAM4 general circulation model, *J. Geophys. Res.*, **102**, 25,751-762.

Miyahara S., Y. Yoshida, Y. Miyoshi, 1993: Diurnal coupling of the lower and upper atmosphere by tides and gravity waves, *J. Atmos. Terr. Phys.*, **55**, 1039-1053.

Müller, K.M., U. Langematz, S. Pawson, 1997: The stratopause semiannual oscillation in the Berlin troposphere-stratosphere-mesosphere GCM, *J. Atmos. Sci.*, **54**, 2749-2759.

Nissen, K.M., P. Braesicke, U. Langematz, 2000: QBO, SAO, and tropical waves in the Berlin TSM GCM: Sensitivity to radiation, vertical resolution, and convection, *J. Geophys. Res.*, **105**, 24,771-790.

Nordeng, T. E., 1994: Extended versions of the convective parameterization scheme at ECMWF and their impact on the mean and transient activity of the model in the tropics, *ECMWF Technical Memorandum, 206*, 41 pp.

Numaguti, A., 1993: Dynamics and energy-balance of the Hadley circulation and the tropical precipitation zones - significance of the distribution of evaporation, *J. Atmos. Sci.*, **50**, 1874-1887.

Pawson, S., U. Langematz, G. Radek, U. Schlese, and P. Strauch, 1998: The Berlin troposphere-stratosphere-mesosphere GCM: Sensitivity to physical parameterizations, *Q. J. R. Meteorol. Soc.*, **124**, 1343-1371.

Pawson, S., et al., 2000: The GCM-Reality Intercomparison Project for SPARC (GRIPS): scientific issues and initial results, *Bull. Am. Meteorol. Soc.*, **81**, 781-796.

Pfister, L., S. Scott, M. Loewenstein, S. Bowen, and M. Legg, 1993: Mesoscale disturbances in the tropical stratosphere excited by convection: observations and effects on the stratospheric momentum budget, *J. Atmos. Sci.*, **50**, 1058-1075.

Portnyagin, Y. I., and T. V. Solovieva, 1997: The role of vertical momentum fluxes in maintaining global meridional circulation in the lower thermosphere/upper mesosphere, *J. Atmos. Solar-Terr. Phys*, **59**, 511-525.

Randall, D. and D.-M. Pan, 1993: Implementation of the Arakawa-Schubert cumulus parameterization with a prognostic closure. *The representation of cumulus convection in numerical models, Meteorol. Monogr., 24*, No. 46, *Am. Meteorol. Soc.*, 145-150.

Randel, W. J., and F. Wu, 1996: Isolation of the ozone QBO in SAGE II data by singular-value decomposition, *J. Atmos. Sci.*, **53**, 2546–2559.

Ray, E.A., M. J. Alexander, and J. R. Holton, 1998: An analysis of the structure and forcing of

the equatorial semiannual oscillation in zonal wind, *J. Geophys. Res.*, **103**, 1759-1774.

Ricciardulli, L., and R. R. Garcia, 2000: The excitation of equatorial waves by deep convection in the NCAR Community Climate Model (CCM3), *J. Atmos. Sci.*, **57**, 3461-3487.

Salby M. L., and R. R. Garcia, 1987: Transient response to localized episodic heating in the tropics. Part I: Excitation and short-time near field behavior, *J. Atmos. Sci.*, **44**, 458-498.

Salby, M. L., D. L. Hartmann, P. L. Bailey, and J. C. Gelle, 1984: Evidence for equatorial Kelvin modes in Nimbus-7 LIMS. *J. Atmos. Sci.*, **41**, 209-236.

Sassi, F., and R. R. Garcia, 1997: The role of equatorial waves forced by convection in the tropical semiannual oscillation, *J. Atmos. Sci.*, **54**, 1925-1942.

Sassi, F., R.R. Garcia, B.A. Boville, and H. Liu, 2002: On temperature inversions and the mesospheric surf zone. *J. Geophys. Res.*, , in press.

Sato K., and T. J. Dunkerton, 1997: Estimates of momentum flux associated with equatorial Kelvin and gravity waves, *J. Geophys. Res.*, **102**, 26,247-261.

Scaife, A.A., N. Butchart, C. D. Warner, D. Stainforth, W. Norton, and J. Austin, 2000: Realistic Quasi-Biennial Oscillations in a simulation of the global climate, *Geophys. Res. Lett.*, **27**, 3481-3484.

Shepherd, T.G., J. N. Koshyk, and K. Ngan, 2000: On the nature of large-scale mixing in the stratosphere and mesosphere, *J. Geophys. Res.*, **105**, 12,433-446.

Shibata, K., H. Yoshimura, M. Ohizumi, M. Hosaka, and M. Sugi, 1999: A simulation of troposphere, stratosphere and mesosphere with an MRI/JMA98 GCM, *Pap. Meteorol. and Geophys.*, **50,** 15-53.

Takahashi, M., 1996: Simulation of the stratospheric quasi-biennial oscillation using a general circulation model, *Geophys. Res. Lett.*, **23**, 661-664.

Takahashi, M., 1999: Simulation of the quasi-biennial oscillation in a general circulation model, *Geophys. Res. Lett.*, **26**, 1307-1310.

Takahashi, M., N. Zhao, and T. Kumakura, 1997: Equatorial waves in a general circulation model simulating a quasi biennial oscillation. *J. Meteor. Soc. Japan*, **75**, 529-540.

Tiedtke, M., W. A. Heckley, J. Slingo, 1988: Tropical forecasting at ECMWF - The influence of physical parameterization on the mean structure of forecasts and analyses, *Q. J. R. Meteorol. Soc.*, **114**, 639-664.

Tiedtke, M., 1989: A comprehensive mass flux scheme for cumulus parameterization in large-scale models, *Mon. Weather Rev.*, **117**, 1779-1800.

Tokioka, T., and I. Yagai, 1987: Atmospheric tides appearing in a global atmospheric general circulation model, *J. Meteor. Soc. Japan,* **65**, 423-438.

Wallace, J.M., and V.E. Kousky, 1968: Observational evidence of Kelvin waves in the tropical stratosphere, *J. Atmos. Sci.*, **25**, 900–907.

Warner, C.D., and M. E. McIntyre, 1999: Toward an ultra-simple spectral gravity wave parameterization for general circulation models, *Earth Planets and Space*, **51**, 475-484.

Williams, C. R., and S. K. Avery, 1996: Diurnal nonmigrating tidal oscillations forced by deep convective clouds, *J. Geophys. Res.*, **101**, 4079-4092.

Williamson, D. L., and J. G. Olson, 1994: Climate simulations with a semi-Lagrangian version of the NCAR Community Climate Model, *Mon. Weather Rev.*, **122**, 1594-1610.

Yanai, M., and T. Maruyama, 1966: Stratospheric wave disturbances propagating over the equatorial Pacific, *J. Meteor. Soc. Japan,* **44**, 291-294.

Zhang, G. J., and N. A. McFarlane, 1995: Sensitivity of climate simulations to the parameterization of cumulus convection in the Canadian Climate Center General-Circulation Model, *Atmosphere-Ocean*, **33**, 407-446.

T. Horinouchi, Radio Science Center for Space and Atmosphere, Kyoto University, Uji, 611-0011, Japan. (horinout@kurasc.kyoto-u.ac.jp)

Received _____

[1]Radio Science Center for Space and Atmosphere, Kyoto University, Uji, Japan

[2]Data Assimilation Office, NASA GSFC, Greenbelt, MD, USA; Goddard Earth Sciences and Technology Center, UMBC, Baltimore, USA

[3]Meteorological Research Institute, Tsukuba, Japan

[4]Freie Universität Berlin, Berlin, Germany

[5]Max-Planck-Institut für Meteorologie, Hamburg, Germany

[6]NCAR, Boulder, Colorado, USA

[7]GFDL, Princeton, New Jersey, USA

[8]University of Hawaii, Honolulu, Hawaii, USA

[9]York University, Toronto, Ontario, Canada

[10]Met Office, Bracknell, UK

Table 1. Models used in the study

Name	Group and location	Reference
MRI/JMA98	MRI, Tsukuba, Japan and JMA	Shibata et al.[1999]
FUB	Freie Univ. Berlin, Germany	Pawson et al. [1998]
		Langematz [2000]
MAECHAM4	MPI, Hamburg, Germany	Manzini et al. [1997]
UKMO	Met Office, Bracknell, UK	Cullen [1993], Scaife et al. [2000]
MACCM3	NCAR, Boulder, CO, USA	Kiehl et al.[1998],
		Williamson and Olson [1994]
CMAM	Canadian Middle Atmosphere Model	Beagley et al. [1997]
FVCCM	NCAR and NASA GSFC	Kiehl et al.[1998], Lin and Rood [1996]
	(CCM3 with Lin-Rood dynamics)	
SKYHI N30L40	GFDL, Princeton, USA	Hamilton et al. [1995]
SKYHI N45L80	GFDL, Princeton, USA	Hamilton et al. [2001]
AGCM5-HY98	GFD Dennou Club, Japan	Horinouchi and Yoden [1998]
	(aqua-planet, experimental)	

Table 2. Summary of grid specification of the models.

model	formulation	horizontal resolution	# of levels	top hPa	Δz (km) in lower strat.
MRI/JMA98	spectral	T42	45	0.01	2
FUB	spectral	T21	34	0.01	2-3
MAECHAM4	spectral	T42	39	0.01	1.7-2.3
UKMO	B-grid	3.75x2.5	55	0.01	1.3
MACCM3	semi-Lag.	T42	54	0.01	1.1-1.5
CMAM	spectral	T32	50	0.001	1.7-2.3
FVCCM	Lin&Rood	144x91	54	0.01	1.1-1.5
SKYHI N30L40	A-grid	3.6x3	40	0.01	1.6-2
SKYHI N45L80	A-grid	2.4x2	80	0.01	0.8-1
AGCM5-HY98	spectral	T42	40	1	0.7

Table 3. Summary of physical specification and miscellaneous aspects of the models.

model	cumulus parameterization	Gravity-wave drag	seasonal & diurnal cycles	output Δt (hr)	Has QBO?
MRI/JMA98	Progn-AS	orographic	yes & yes	3	no
FUB	Kuo	none	yes & yes	3	no
MAECHAM4	Tiedtke/Nordeng	orographic & Hines	yes & yes	3	no
UKMO	GR	orographic & WM	yes & yes	3	yes
MACCM3	ZM	orographic & $c \neq 0$ prescribed	yes & yes	6	no
CMAM	ZM	orographic	yes & yes	3	no
FVCCM	ZM	orographic	yes & yes	3	no
SKYHI N30L40	MCA	none	yes & no	3	no
SKYHI N45L80	MCA	none	yes & no	3	yes
AGCM5-HY98	MCA	none	no & no	3	yes

Table 4. $|F^{(}z)|$ averaged between 10N and 10S at a level close to 65 hPa for various frequency ranges [10^{-3} J]. Also shown are observational estimates taken from Sato and Dunkerton [1997] and Hertzog and Vial [2001]. Note that comparison with the observational estimates is limited (see the text for details).

ω (cpd)	0.33–0.97	0.97–1.03	1.03-3.3
MRI/JMA98	0.10	0.038	0.074
FUB	0.16	0.026	0.035
MAECHAM4	0.20	0.099	0.22
MACCM3	0.032	0.056	0.012
CMAM	0.096	0.070	0.075
FVCCM	0.0089	0.042	0.0056
UKMO	0.053	0.10	0.022
SKYHI N30L40	0.64		0.38
SKYHI N45L80	0.52		1.6
AGCM5	1.1		0.82
SD97	0.7∼1.3		
SD97 × 0.3	0.2∼0.4		
HV01			0.2

Table 5. Summary of cumulus parameterizations in the models

model	method	shallow/ midlevel	mass flux?	closure	trigger
MRI/JMA98	Progn-AS	included	yes	CWF	CWF > 0
FUB	Kuo	Tiedtke/Nordeng	no	q supply	q supply>0
MAECHAM4	Tiedtke	included	yes	CAPE	q supply>0
UKMO	GR	included	yes	(see the text)	
CMAM	ZM	none	yes	CAPE	CAPE > 0
FVCCM/MACCM3	ZM	Hack [1994]	yes	CAPE	CAPE > 0
SKYHI	MCA	none	no	stability	$\Gamma_m \sim< 0$
AGCM5-HY98	MCA	none	no	stability	$\Gamma_m \sim< 0$

Figure 1. Time-height section of zonal and monthly mean zonal wind averaged between 10°N and 10°S for selected models (MRI/JMA98, MACCM3, and SKYHI-N30L40) and its height profile for January for other models (lower-right panel).

Figure 2. Mean precipitation (mm/day) for each model over the DJF period except for the AGCM5, for which an average over a 60-day period is shown. Also shown in the bottom panel is a climatology derived from the GPCP estimate from 1987-1999.

Figure 3. Same as in Fig. 2, but for zonal mean.

Figure 4. Two-dimensional, zonal wavenumber-frequency spectra of precipitation rate (left panels, in m^2s^{-2}=1.34× $10^{-16}mm^2day^{-2}$); $\tilde{F}^{(z)}$ at a level close to 65 hPa for each model (mid panels, in Pa); $\tilde{F}^{(z)}$ at a level close to 1 hPa for each model (right panels). Seven models were selected for conciseness. The spectra were calculated at each longitude, averaged afterwards between 10°S and 10°N, and plotted in the "energy-content" form after some smoothing (see Appendix). Dotted lines show zonal phase velocities. Thick solid lines in the mid and right panels show the time-averaged zonal mean zonal wind of the same vertical level for each model. Shading with thin solid lines in the right panels are made between the maximum and minimum of the time-averaged zonal mean zonal wind from 100 hPa to the level for which $\tilde{F}^{(z)}$ are shown.

Figure 5. Frequency (in cpd) spectra of precipitation ($m^2s^{-2}day$; not in the energy-content form). The calculation is made for the entire 3-month period (2 months for AGCM5), but the spectra are shown only above 0.05 cpd (corresponding to the period of 20 days). Also shown are observational estimates of precipitation spectra (see Section 3.3 for details): (line with '+' marks) from TOGA-COARE meteorological radars, (line with triangular marks) with the RG2000 for the TOGA-COARE region and period, (black thin solid line) the one obtained by RG2000, which is averaged over the entire equatorial region between 15°N and 15°S. Dotted lines with a slope of -1 are drawn in order to facilitate to see how the spectra would look like if they were plotted in the energy-content form. Dashed lines having slopes of -3 and $-5/3$ are drawn just for reference.

Figure 6. Same as in Fig. 5, but for (upper-left) temperature (K^2day), (upper-right) vertical pressure velocity (Pa^2s^{-2}day), and (lower-left) eastward-moving and (lower-right) westward-moving components of $F^{(z)}$ (Pa^2day) at a level close to 65 hPa for each model.

Figure 7. Vertical distribution (as functions of pressure in hPa) of kinetic energy (m^2s^{-2}) defined as $u^2 + v^2$ averaged between 10°N and 10°S for disturbances classified in terms of zonal wavenumber and frequency ranges: westward-moving disturbances in total (thin solid lines), non-migrating westward-moving diurnal tides defined by the integration over $s \leq -2$ and $0.97 < \omega < 1.03$ (dotted lines), migrating diurnal tides with $s = -1$ and $0.97 < \omega < 1.03$ (dash-dotted lines), eastward-moving disturbances in total (thick solid lines), eastward-moving disturbances from $+1 \leq s \leq +3$ and $\omega < 0.3$ cpd (thick-dashed lined), and eastward-moving non-migrating diurnal tides defined as the integration over $s \geq +1$ and d $0.97 < \omega < 1.03$ cpd. Six models were selected for conciseness. Note that the abscissae are shifted by 3 orders of magnitude between westward- and eastward-moving disturbances.

Figure 8. Same as in Fig. 7, but for $F^{(z)}$. The sign of $F^{(z)}$ of eastward-moving disturbances are negated, since it is negative for upward-propagating waves.

Figure 9. Zonal wavenumber distribution of $F^{(z)}$ (Pa) at a level close to 65 hPa for each model. Plots here are made in the log-log coordinate without multiplying $|s|$. They are obtained by integrating the space-time spectra with respect to ω from 0.1 to 0.3 cpd (upper-left), from 0.3 to 0.97 cpd (upper-right), from 0.97 to 1.03 cpd (lower-left), and from 1.03 to 4 cpd (lower-right). Only positive (negative) values are shown for westward- (eastward-) moving disturbances. Note that the lower-right panel is to show the contribution of the diurnal tides to the EP flux, where models without the diurnal cycle in radiation are excluded (SKYHI and AGCM5).

Figure 10. Same as in Fig. 9, but for a level close to 1 hPa for each model.

Figure 11. EP flux divergence and the tendency of zonal wind averaged between 10°N and S over the latter half of the DJF period (ms^{-2}). The tendency is shown by thick-dashed lines, and the total EP flux divergence is shown by thin solid lines. Also shown are contributions to the latter from various wavenumber-frequency ranges of eastward-moving disturbances: $1.03 < \omega \leq 2$ cpd (thin dotted lines), $0.97 < \omega < 1.03$ cpd (thick dotted lines), $s = 1$ to 3 and $\omega < 0.3$ cpd (thick dashed lines), $s = 1$ and $\omega < 0.2$ (thin dashed lines), and $s \geq 4$ and $\omega < 0.9$ (dash-dotted lines).

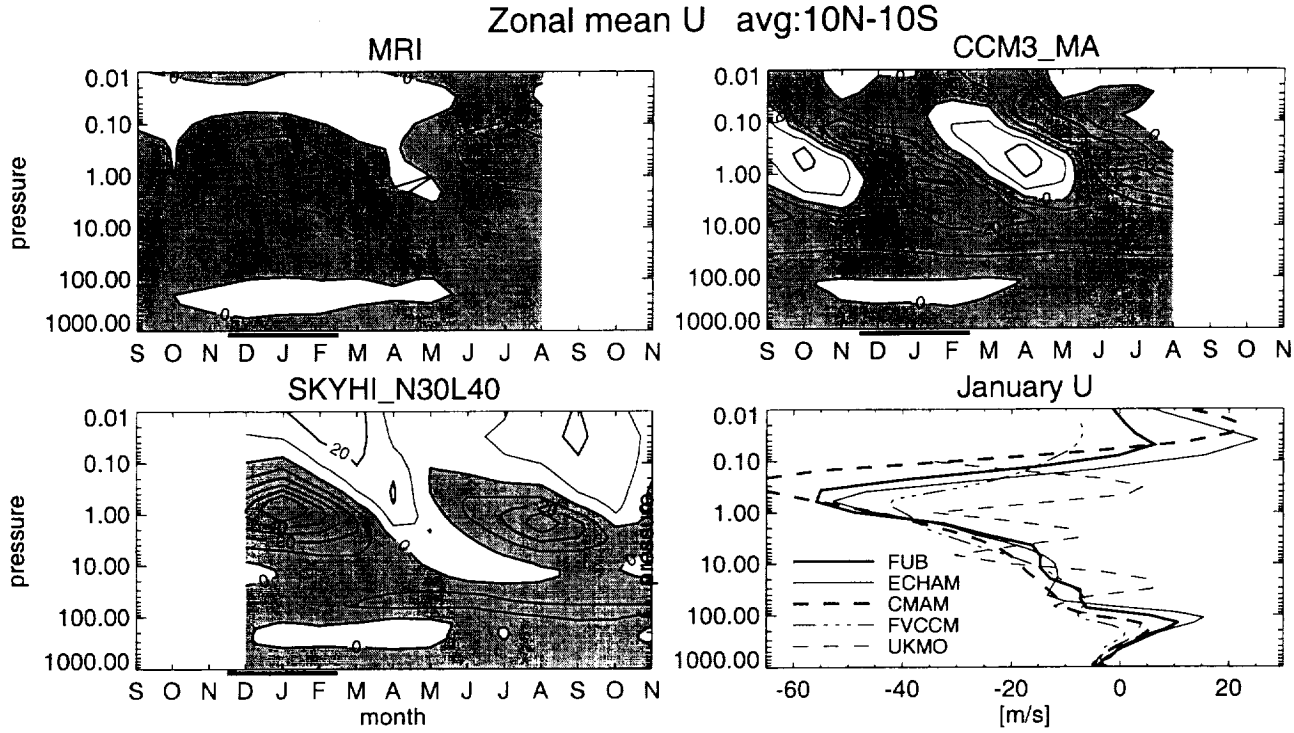
Zonal mean U avg:10N-10S
MRI
CCM3_MA
SKYHI_N30L40
January U
pressure
0.01
0.10
1.00
10.00
100.00
1000.00
S O N D J F M A M J J A S O N
month
FUB
ECHAM
CMAM
FVCCM
UKMO
-60
-40
-20
0
20
[m/s]

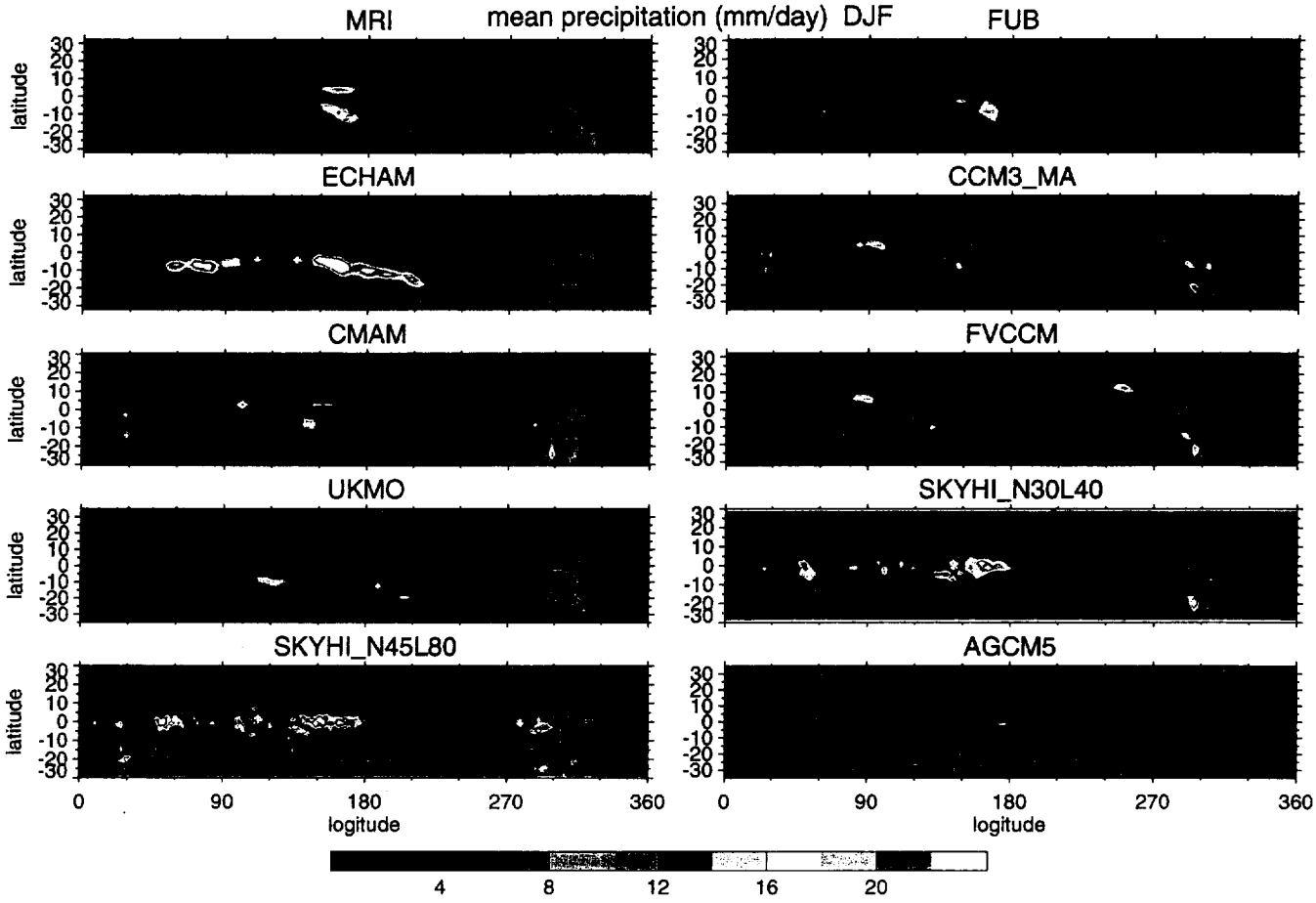
mean precipitation (mm/day) DJF
MRI
FUB
ECHAM
CCM3_MA
CMAM
FVCCM
UKMO
SKYHI_N30L40
SKYHI_N45L80
AGCM5
latitude
logitude
30
20
10
0
-10
-20
-30
0
90
180
270
360
4
8
12
16
20

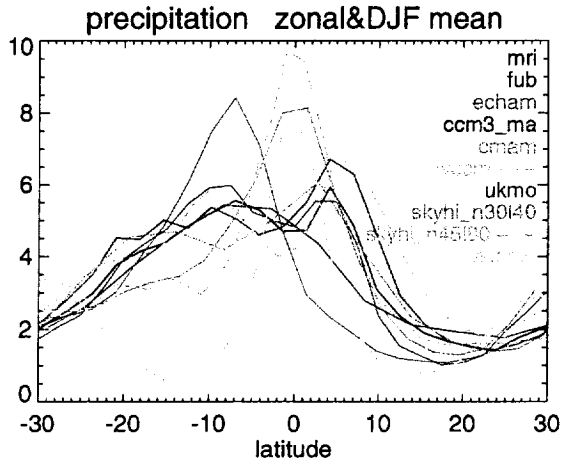
precipitation zonal&DJF mean
10
8
6
4
2
0
-30
-20
-10
0
10
20
30
latitude
mri
fub
echam
ccm3_ma
cmam
ukmo
skyhi_n30l40

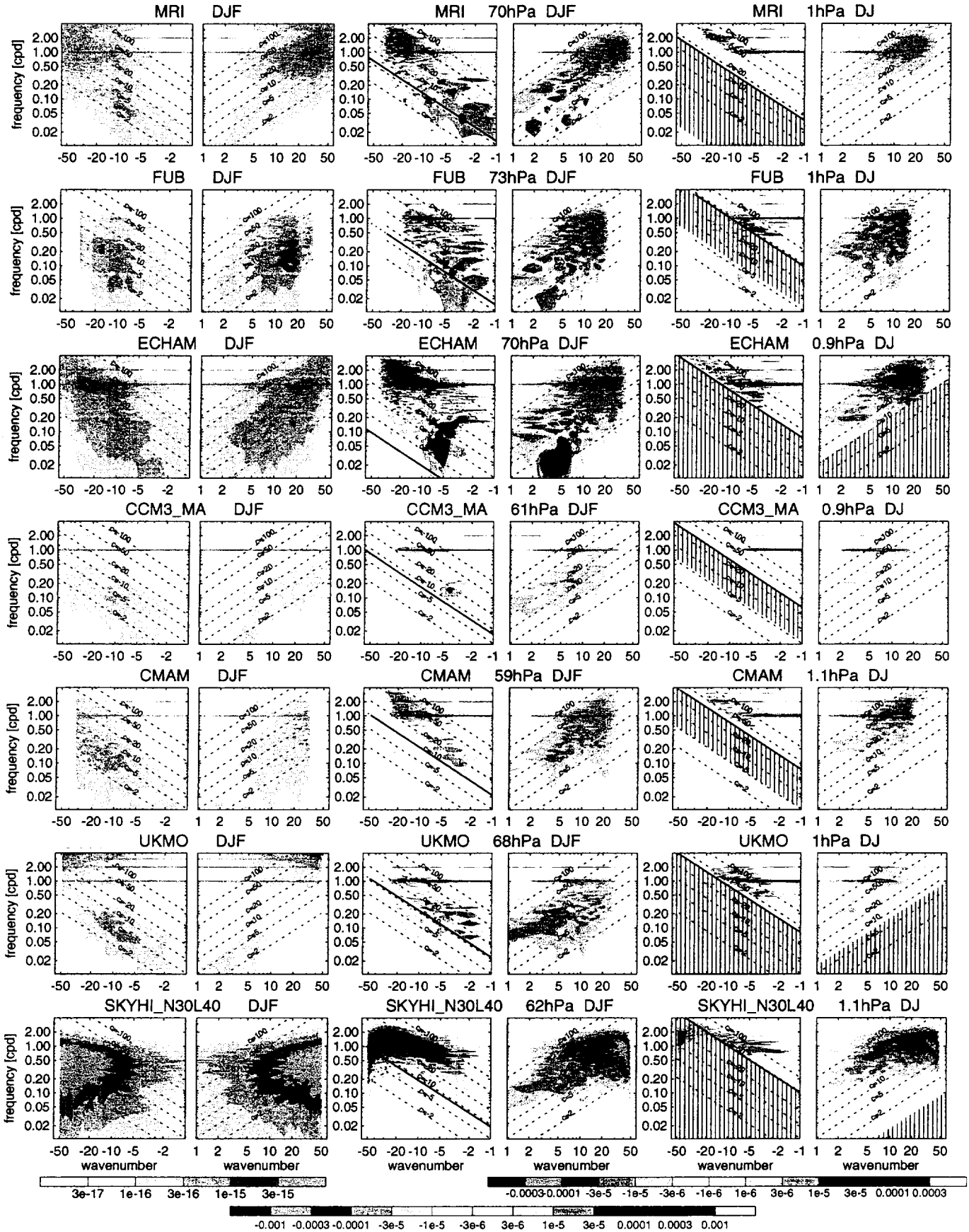
MRI DJF
MRI 70hPa DJF
MRI 1hPa DJ
FUB DJF
FUB 73hPa DJF
FUB 1hPa DJ
ECHAM DJF
ECHAM 70hPa DJF
ECHAM 0.9hPa DJ
CCM3_MA DJF
CCM3_MA 61hPa DJF
CCM3_MA 0.9hPa DJ
CMAM DJF
CMAM 59hPa DJF
CMAM 1.1hPa DJ
UKMO DJF
UKMO 68hPa DJF
UKMO 1hPa DJ
SKYHI_N30L40 DJF
SKYHI_N30L40 62hPa DJF
SKYHI_N30L40 1.1hPa DJ
frequency [cpd]
wavenumber
3e-17 1e-16 3e-16 1e-15 3e-15
-0.0003 -0.0001 -3e-5 -1e-5 -3e-6 -1e-6 1e-6 3e-6 1e-5 3e-5 0.0001 0.0003
-0.001 -0.0003 -0.0001 -3e-5 -1e-5 -3e-6 3e-6 1e-5 3e-5 0.0001 0.0003 0.001

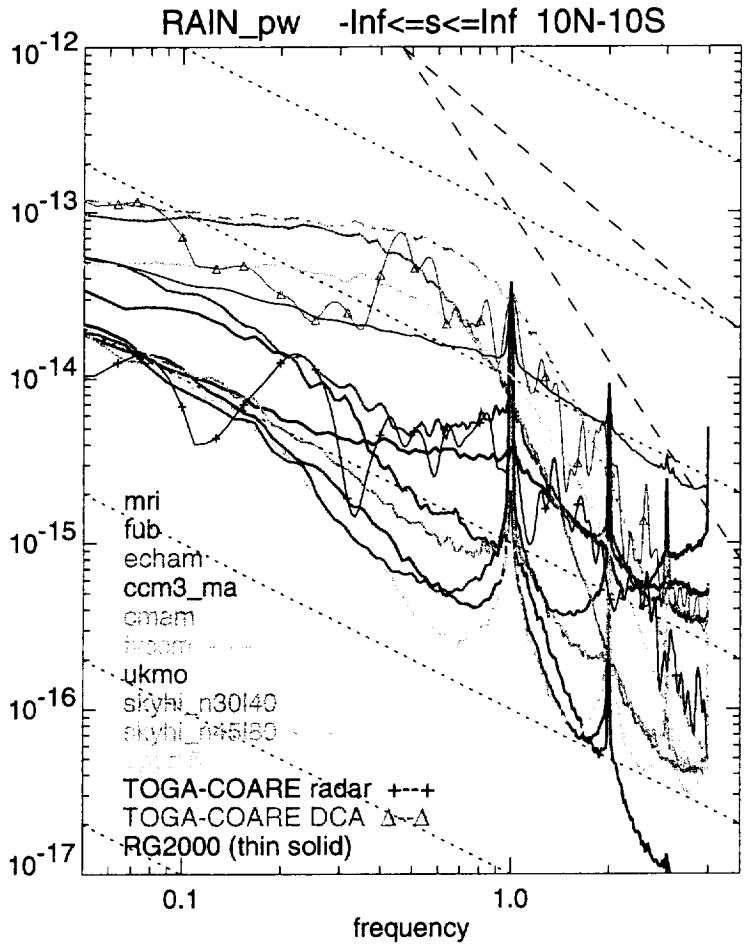
RAIN_pw -Inf<=s<=Inf 10N-10S
10^-12
10^-13
10^-14
10^-15
10^-16
10^-17
mri
fub
echam
ccm3_ma
cmam
ukmo
skyhi_n30l40
TOGA-COARE radar +--+
TOGA-COARE DCA Δ--Δ
RG2000 (thin solid)
0.1
1.0
frequency

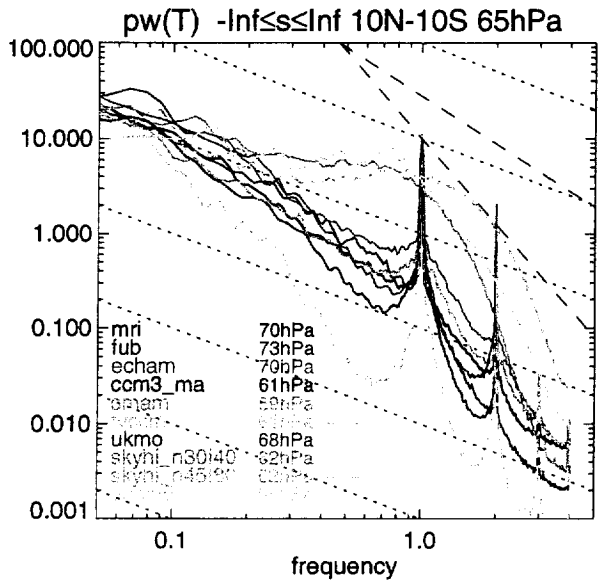
pw(T) -Inf≤s≤Inf 10N-10S 65hPa
100.000
10.000
1.000
0.100
0.010
0.001
mri 70hPa
fub 73hPa
echam 70hPa
ccm3_ma 61hPa
ukmo 68hPa
skyhi_n30l40 62hPa
0.1
1.0
frequency

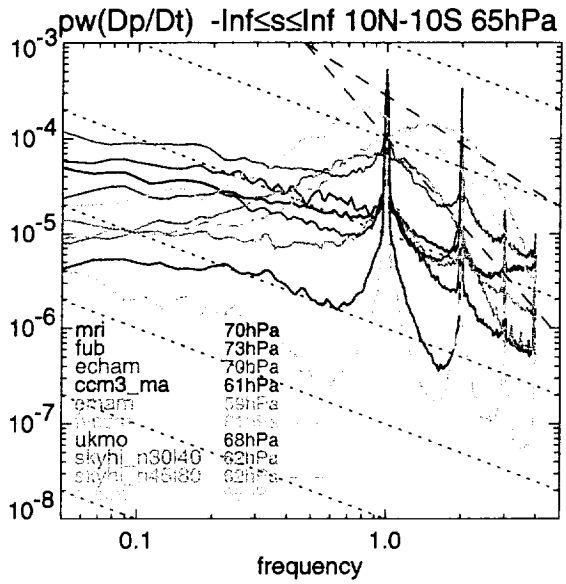
pw(Dp/Dt) -Inf≤s≤Inf 10N-10S 65hPa
10^{-3}
10^{-4}
10^{-5}
10^{-6}
10^{-7}
10^{-8}
mri 70hPa
fub 73hPa
echam 70hPa
ccm3_ma 61hPa
ukmo 68hPa
skyhi_n30l40 62hPa
0.1
1.0
frequency

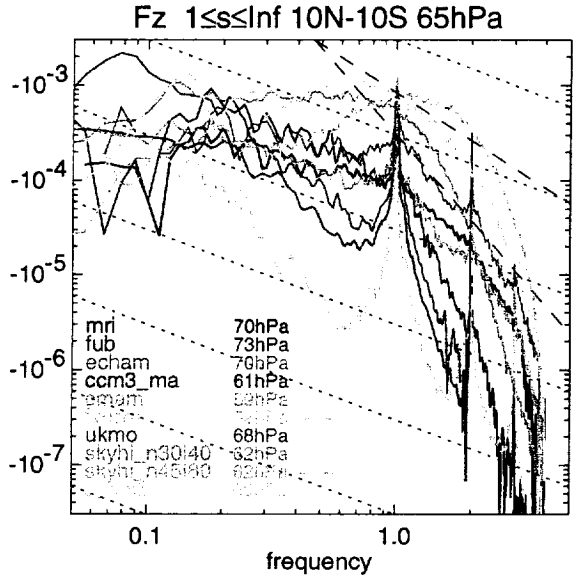
Fz 1≤s≤Inf 10N-10S 65hPa
-10^{-3}
-10^{-4}
-10^{-5}
-10^{-6}
-10^{-7}
mri 70hPa
fub 73hPa
echam 70hPa
ccm3_ma 61hPa
ukmo 68hPa
skyhi_n30l40 62hPa
0.1
1.0
frequency

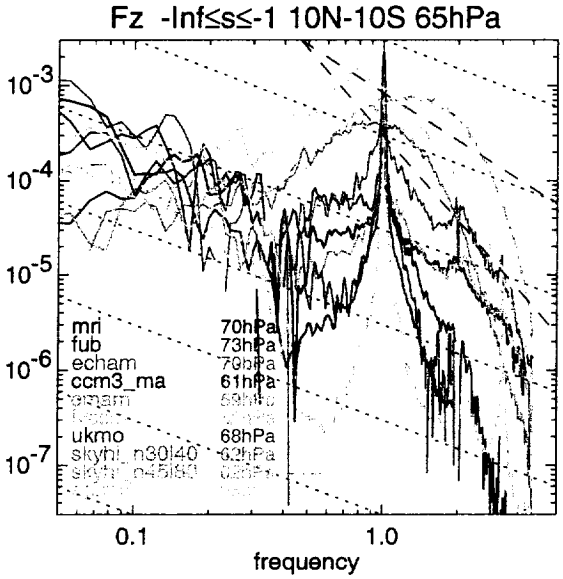
Fz -Inf≤s≤-1 10N-10S 65hPa
10^{-3}
10^{-4}
10^{-5}
10^{-6}
10^{-7}
mri 70hPa
fub 73hPa
echam 70hPa
ccm3_ma 61hPa
ukmo 68hPa
skyhi_n30l40 62hPa
0.1
1.0
frequency

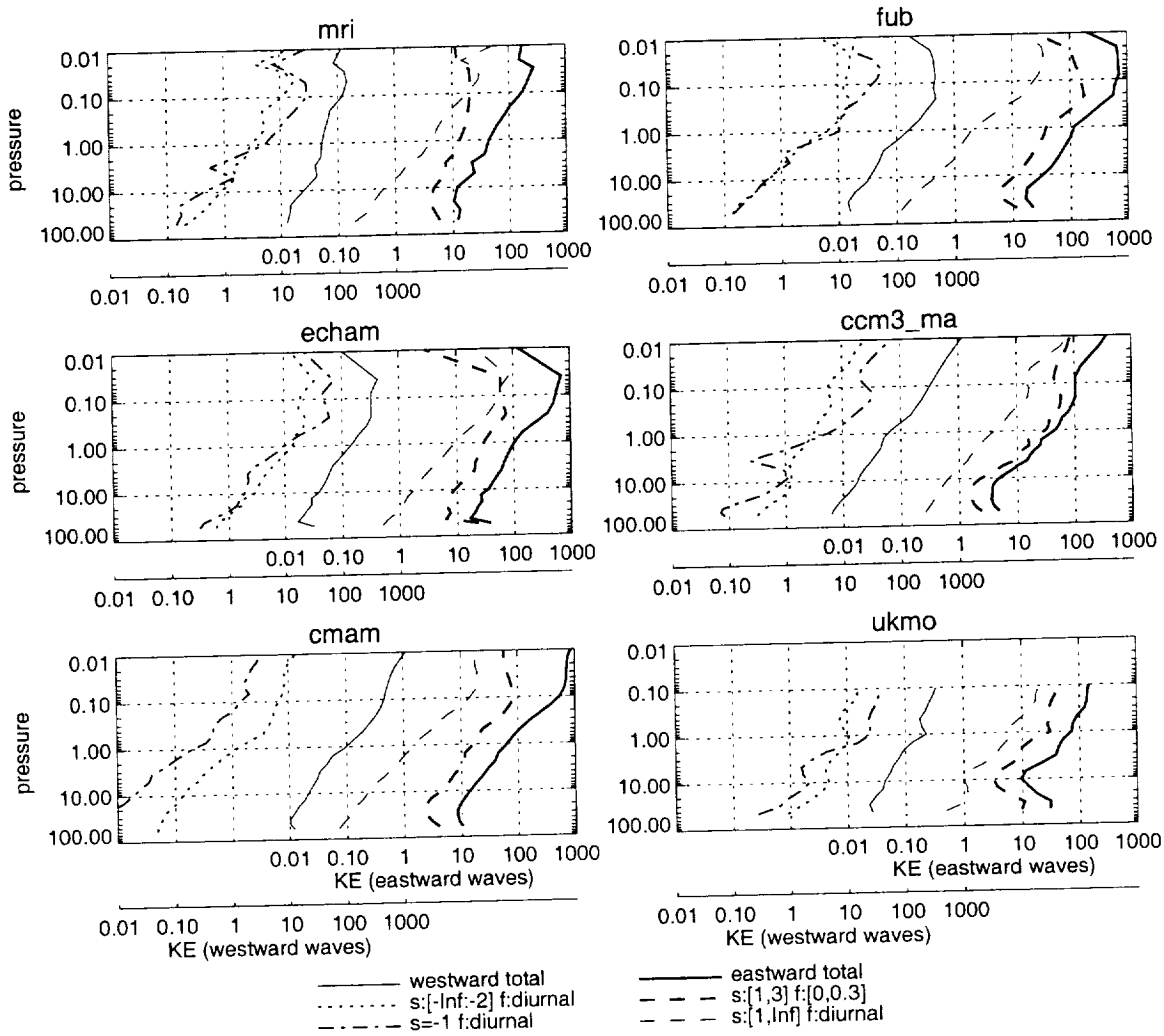
mri
fub
echam
ccm3_ma
cmam
ukmo
pressure
0.01
0.10
1.00
10.00
100.00
0.01 0.10 1 10 100 1000
KE (eastward waves)
KE (westward waves)
westward total
s:[-Inf:-2] f:diurnal
s=-1 f:diurnal
eastward total
s:[1,3] f:[0,0.3]
s:[1,Inf] f:diurnal

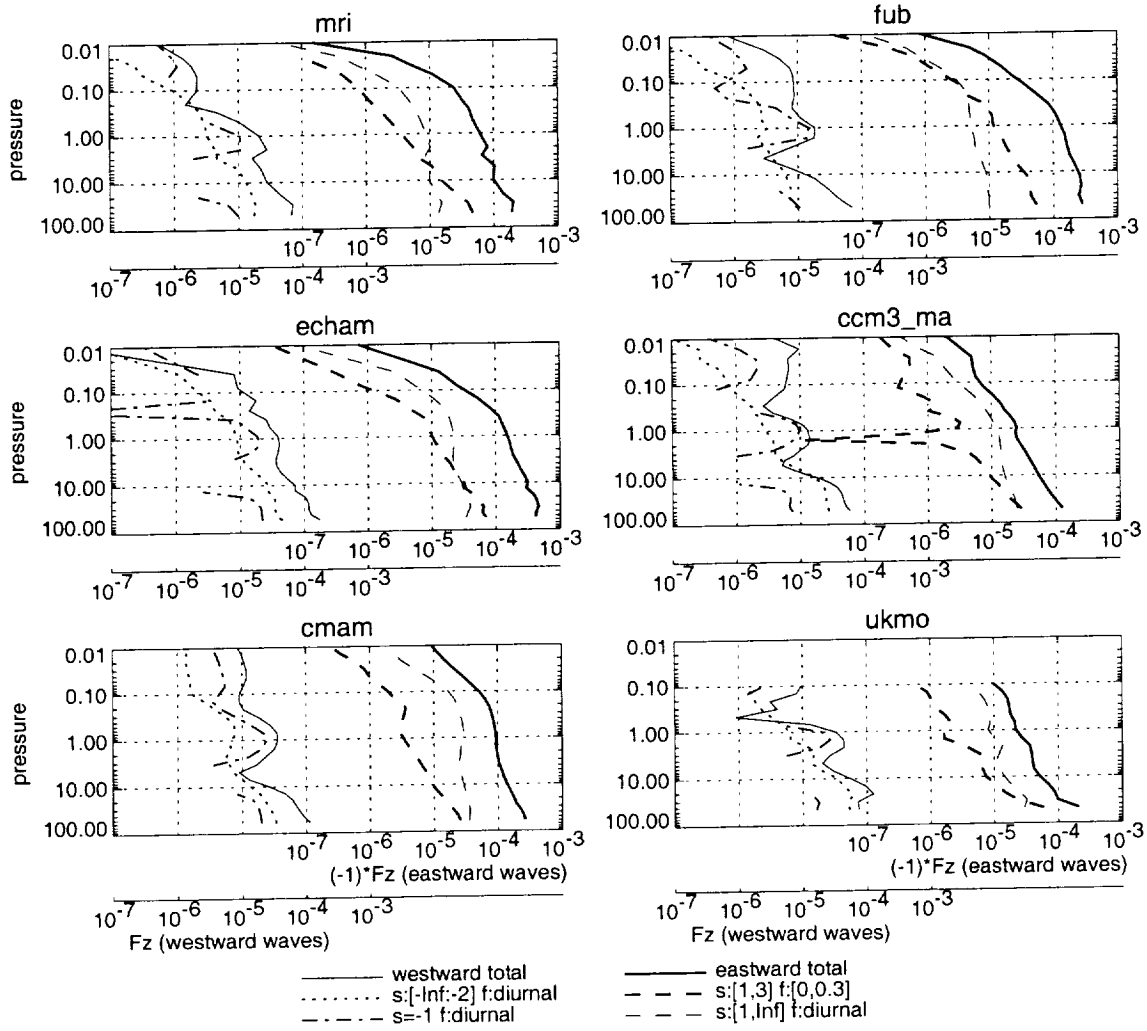
mri
fub
echam
ccm3_ma
cmam
ukmo
pressure
0.01
0.10
1.00
10.00
100.00
10^{-7} 10^{-6} 10^{-5} 10^{-4} 10^{-3}
(-1)*Fz (eastward waves)
Fz (westward waves)
westward total
s:[-Inf:-2] f:diurnal
s=-1 f:diurnal
eastward total
s:[1,3] f:[0,0.3]
s:[1,Inf] f:diurnal

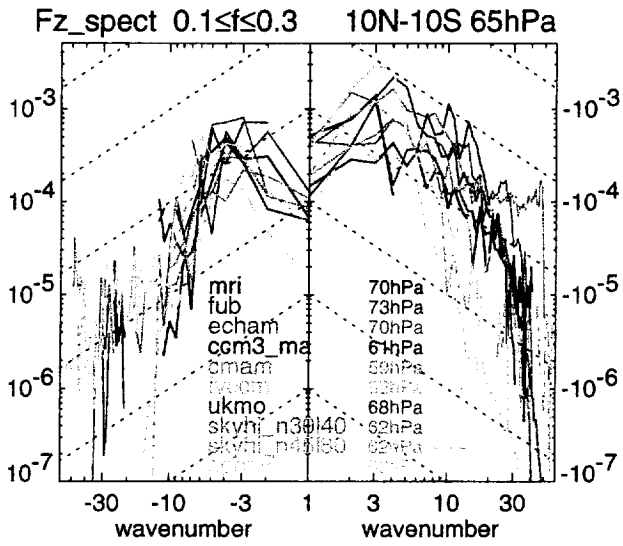
Fz_spect 0.1≤f≤0.3 10N-10S 65hPa
mri 70hPa
fub 73hPa
echam 70hPa
ccm3_ma 61hPa
cmam 59hPa
ukmo 68hPa
skyhi_n30l40 62hPa
wavenumber
wavenumber

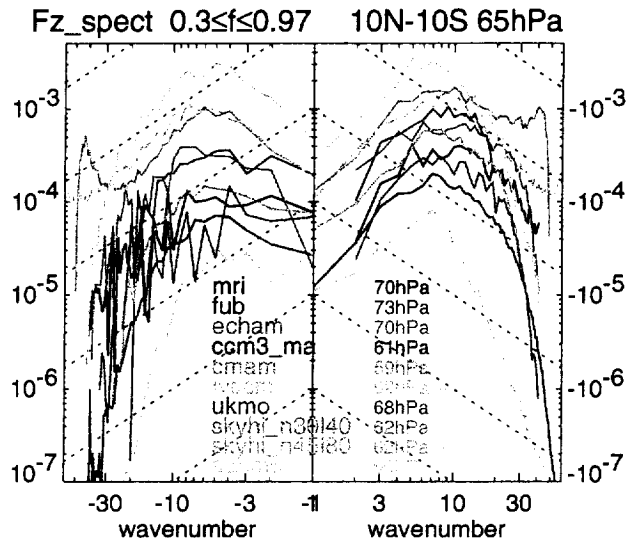
Fz_spect 0.3≤f≤0.97 10N-10S 65hPa
mri 70hPa
fub 73hPa
echam 70hPa
ccm3_ma 61hPa
cmam 59hPa
ukmo 68hPa
skyhi_n30l40 62hPa
wavenumber
wavenumber

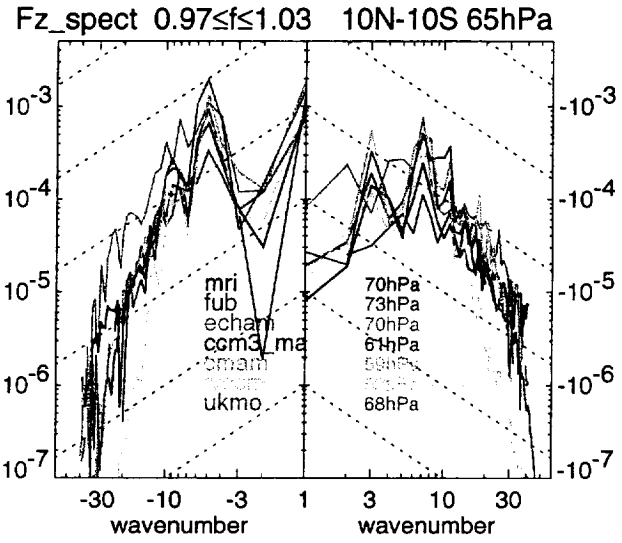
Fz_spect 0.97≤f≤1.03 10N-10S 65hPa
mri 70hPa
fub 73hPa
echam 70hPa
ccm3_ma 61hPa
cmam 59hPa
ukmo 68hPa
wavenumber
wavenumber

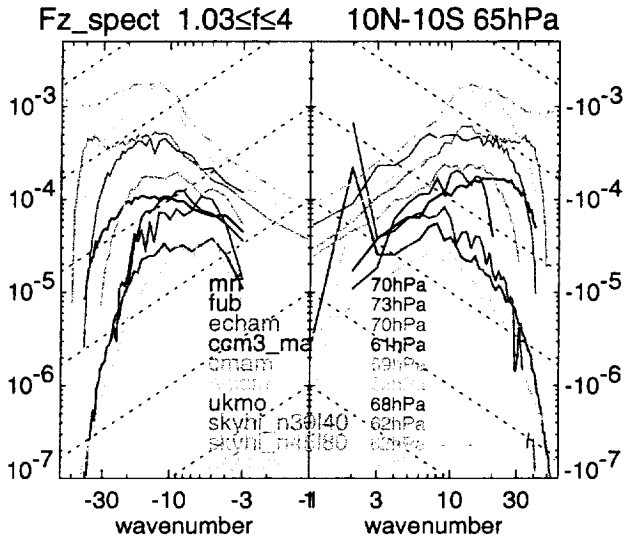
Fz_spect 1.03≤f≤4 10N-10S 65hPa
mri 70hPa
fub 73hPa
echam 70hPa
ccm3_ma 61hPa
cmam 59hPa
ukmo 68hPa
skyhi_n30l40 62hPa
wavenumber
wavenumber

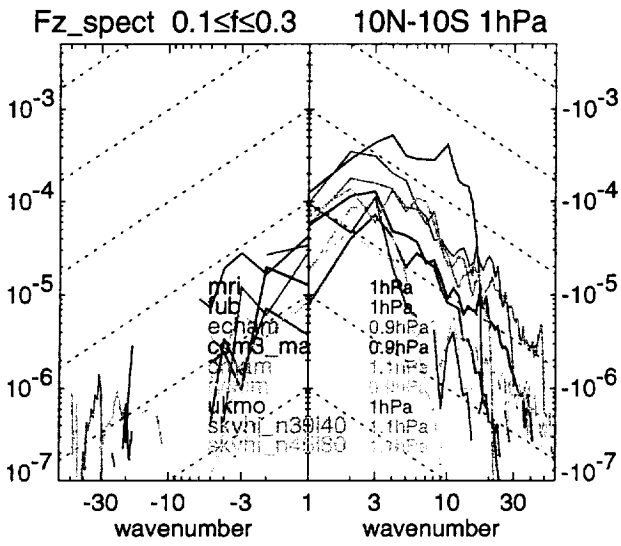
Fz_spect 0.1≤f≤0.3 10N-10S 1hPa
10^-3
10^-4
10^-5
10^-6
10^-7
-10^-3
-10^-4
-10^-5
-10^-6
-10^-7
mri 1hPa
fub 1hPa
echam 0.9hPa
ccm3_ma 0.9hPa
cmam 1.1hPa
ukmo 1hPa
skyhi_n30l40 1.1hPa
skyhi_n45l80 1.1hPa
-30 -10 -3 1 3 10 30
wavenumber
wavenumber

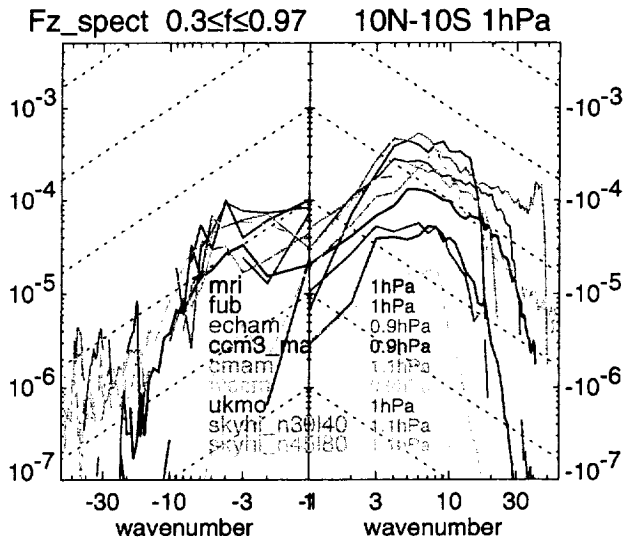
Fz_spect 0.3≤f≤0.97 10N-10S 1hPa
10^-3
10^-4
10^-5
10^-6
10^-7
-10^-3
-10^-4
-10^-5
-10^-6
-10^-7
mri 1hPa
fub 1hPa
echam 0.9hPa
ccm3_ma 0.9hPa
cmam 1.1hPa
ukmo 1hPa
skyhi_n30l40 1.1hPa
skyhi_n45l80 1.1hPa
-30 -10 -3 1 3 10 30
wavenumber
wavenumber

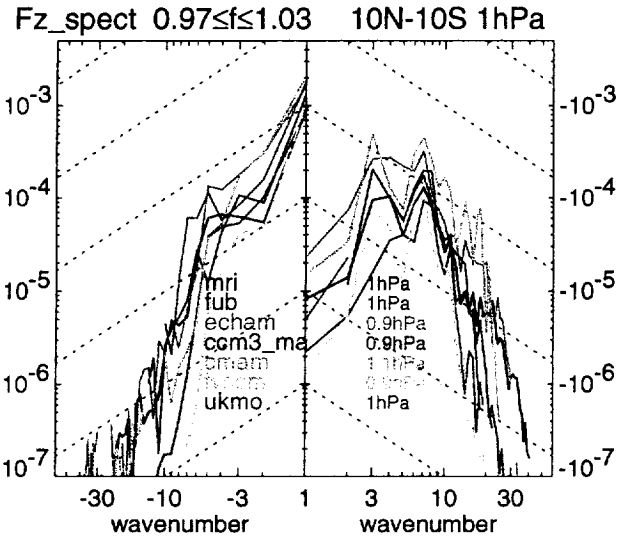
Fz_spect 0.97≤f≤1.03 10N-10S 1hPa
10^-3
10^-4
10^-5
10^-6
10^-7
-10^-3
-10^-4
-10^-5
-10^-6
-10^-7
mri 1hPa
fub 1hPa
echam 0.9hPa
ccm3_ma 0.9hPa
cmam 1.1hPa
ukmo 1hPa
-30 -10 -3 1 3 10 30
wavenumber
wavenumber

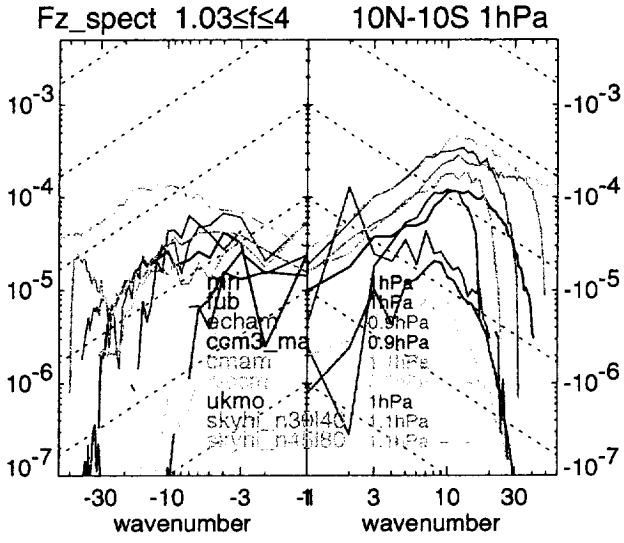
Fz_spect 1.03≤f≤4 10N-10S 1hPa
10^-3
10^-4
10^-5
10^-6
10^-7
-10^-3
-10^-4
-10^-5
-10^-6
-10^-7
mri 1hPa
fub 1hPa
echam 0.9hPa
ccm3_ma 0.9hPa
cmam 1.1hPa
ukmo 1hPa
skyhi_n30l40 1.1hPa
skyhi_n45l80 1.1hPa
-30 -10 -3 1 3 10 30
wavenumber
wavenumber

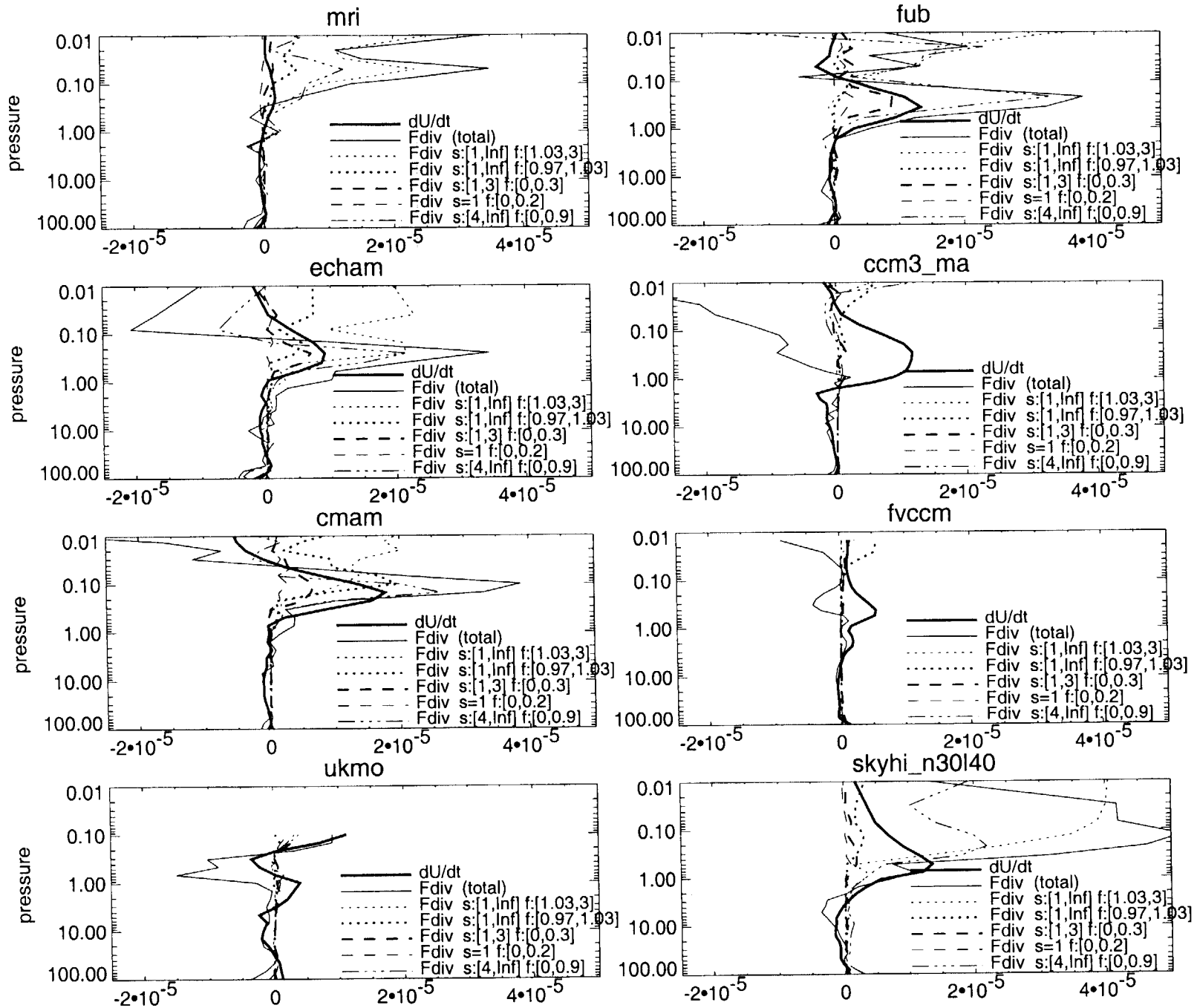
mri
fub
echam
ccm3_ma
cmam
fvccm
ukmo
skyhi_n30l40
pressure
0.01
0.10
1.00
10.00
100.00
-2•10-5
0
2•10-5
4•10-5
dU/dt
Fdiv (total)
Fdiv s:[1,Inf] f:[1.03,3]
Fdiv s:[1,Inf] f:[0.97,1.03]
Fdiv s:[1,3] f:[0,0.3]
Fdiv s=1 f:[0,0.2]
Fdiv s:[4,Inf] f:[0,0.9]